Turbulent Mixing in the Benthic Biolayer of Streams

Stanley Grant[1,1], Jesus Gomez-Velez[2,2], Marco Ghisalberti[3,3], Ian Guymer[4,4], Fulvio Boano[5,5], Kevin Roche[6,6], and Jud Harvey[7,7]

[1]Virginia Tech
[2]Vanderbilt University
[3]University of Western Australia
[4]University of Sheffield
[5]Politechnico di Torino
[6]Institute of Environmental al Research and Water Research
[7]USGS

November 30, 2022

Abstract

In this paper we develop and test a rigorous modeling framework, based on Duhamel's Theorem, for the unsteady one-dimensional transport and mixing of a solute across a flat sediment-water interface (SWI) and through the benthic biolayer of a turbulent stream. The modeling framework is novel in that it allows for depth-varying diffusivity profiles, accounts for the change in porosity across the SWI and captures the two-way coupling between evolving solute concentrations in both the overlying water column and interstitial fluids of the sediment bed. We apply this new modeling framework to an extensive set of previously published laboratory measurements of turbulent mixing across a flat sediment bed, with the goal of evaluating four diffusivity profiles (constant, exponentially declining, and two hybrid models that account for molecular diffusion and enhanced turbulent mixing in the surficial portion of the bed). The exponentially declining profile is superior (based on RMSE, coefficient of determination, AICc, and model parsimony) and its reference diffusivity scales with a dimensionless measure of stream turbulence and streambed permeability called the Permeability Reynolds Number, . The diffusivity's dependence on changes abruptly at , reflecting different modes of mixing below (dispersion) and above (turbulent diffusion) this threshold value. The depth-scale over which the diffusivity exponentially decays is about equal to the thickness of the benthic biolayer (2 to 5 cm), implying that turbulent mixing, and specifically turbulent pumping, may play an outsized role in the biogeochemical processing of nutrients and other contaminants in stream and coastal sediments.

Vertical Structure and Scaling of Turbulent Mixing in the Benthic

Biolayer of Stream and Coastal Sediments

Stanley B. Grant[1,2], Jesus D. Gomez-Velez[3], Marco Ghisalberti[4], Ian Guymer[5], Fulvio Boano[6], Kevin Roche[7], Judson Harvey[8]

[1]Occoquan Watershed Monitoring Laboratory, Department of Civil and Environmental Engineering, Virginia Tech, 9408 Prince William Street, Manassas VA 20110, USA

[2]Center for Coastal Studies, Virginia Tech, 1068A Derring Hall (0420), Blacksburg, VA 24061, USA

[3]Department of Civil and Environmental Engineering, Vanderbilt University, Nashville, TN 37205, USA

[4]Oceans Graduate School, University of Western Australia, Perth, WA, 6009, Australia.

[5]Department of Civil and Structural Engineering, Sir Frederick Mappin Building, Mappin Street, Sheffield, S1 3JD, England

[6]Department of Environment, Land and Infrastructure Engineering, Politecnico di Torino, Torino 10129, Italy.

[7]Institute of Environmental al Research and Water Research, Spanish National Research Council (CSIC), 08034 Barcelona, Spain

[8]United States Geological Survey, Earth System Processes Division, Reston VA, 20192, USA

Corresponding author: Stanley B. Grant (stanleyg@vt.edu)

Key Points:

- A one-dimensional diffusion model, based on Duhamel's Theorem, is developed for turbulent mass transport in the benthic biolayer

- The model reproduces solute transfer above and below the sediment-water interface provided the diffusivity decays exponentially with depth

- Turbulent mixing increases with the Permeability Reynolds Number, and appears to be driven by turbulent pumping

30 **Abstract**

31 In this paper we develop and test a rigorous modeling framework, based on Duhamel's

32 Theorem, for the unsteady one-dimensional transport and mixing of a solute across a flat

33 sediment-water interface (SWI) and through the benthic biolayer of a turbulent stream.

34 The modeling framework is novel in that it allows for depth-varying diffusivity profiles,

35 accounts for the change in porosity across the SWI and captures the two-way coupling

36 between evolving solute concentrations in both the overlying water column and

37 interstitial fluids of the sediment bed. We apply this new modeling framework to an

38 extensive set of previously published laboratory measurements of turbulent mixing across

39 a flat sediment bed, with the goal of evaluating four diffusivity profiles (constant,

40 exponentially declining, and two hybrid models that account for molecular diffusion and

41 enhanced turbulent mixing in the surficial portion of the bed). The exponentially

42 declining profile is superior (based on RMSE, coefficient of determination, AICc, and

43 model parsimony) and its reference diffusivity scales with a dimensionless measure of

44 stream turbulence and streambed permeability called the Permeability Reynolds Number,

45 Re_K. The diffusivity's dependence on Re_K changes abruptly at $\mathrm{Re}_K = 1$, reflecting

46 different modes of mixing below (dispersion) and above (turbulent diffusion) this

47 threshold value. The depth-scale over which the diffusivity exponentially decays is about

48 equal to the thickness of the benthic biolayer (2 to 5 cm), implying that turbulent mixing,

49 and specifically turbulent pumping, may play an outsized role in the biogeochemical

50 processing of nutrients and other contaminants in stream and coastal sediments.

51
52

53

54   **Plain Language Summary**

55   How far and fast pollutants travel downstream is often conditioned on what happens in a

56   thin veneer of biologically active bottom sediments called the benthic biolayer. However,

57   before a pollutant can be removed in the benthic biolayer it must first be transported

58   across the sediment-water interface and through the interstitial fluids of these surficial

59   sediments. In this paper we investigate, through mathematical modeling and an

60   evaluation of previously published experimental data, the role that water column

61   turbulence plays in transporting solutes into and through the benthic biolayer of streams

62   and coastal sediments.

63

1 Introduction

Many physical and biological processes in aquatic ecosystems depend on, or are strongly affected by, turbulent fluid motions at the sediment-water interface (SWI) (Franca and Brocchini, 2015; Grant and Marusic, 2011). Stream turbulence drives the vertical transport of dissolved constituents through the water column (Tomasek et al., 2018; O'Connor and Hondzo, 2008; Hondzo, 1998) imposing an upper limit on the rate that reactive constituents, nitrate for example, can be assimilated and removed by the streambed (Grant et al., 2018a). Stream turbulence also facilitates the transport and mixing of dissolved and fine particulate materials and energy across the SWI and in the benthic biolayer, the upper 5 cm of the streambed where much of the microbial biomass, as well as nutrient and pollutant processing, is concentrated (Tomasek et al., 2018; Knapp et al., 2017; Caruso et al., 2017; Trauth et al., 2014; Harvey et al., 2013; Zarnetske et al., 2011; Battin et al., 2008; Dahm et al., 2002).

At the scale of the benthic biolayer, stream turbulence facilitates mixing in at least two ways (**Figure 1a**): (1) "turbulent pumping" occurs when spatially coherent eddies spawn pressure waves that travel along the SWI and drive temporally oscillating laminar flow across the interface (Kim et al., 2020; Zhong et al., 2016; Boano et al., 2011; Higashino et al., 2009); and (2) "turbulence penetration" occurs when turbulent eddies drive intermittent transport of mass and momentum across the interface (Kim et al., 2020; Roche et al., 2018; Voermans et al., 2017; Reidenbach et al., 2010; Packman et al., 2004). If ripples and dunes are present on the streambed surface, mixing across the benthic biolayer is also facilitated by the advective transport of solutes across the SWI in spatially isolated upwelling and downwelling zones, "bedform pumping" (Azizian et al., 2018;

87   Grant et al., 2014; Fleckenstein et al., 2010; Cardenas et al., 2008; Elliot and Brooks,

88   1997a,b; Thibodeaux and Boyle, 1987)) and the entrapment and release of interstitial

89   fluids associated with bedform migration, "bedform turnover" (Wolke et al., 2020; Zheng

90   et al., 2019; Elliot and Brooks, 1997a,b)). Solute mixing in the streambed is also

91   controlled by molecular diffusion (which smooths out the steep concentration gradients

92   generated by the above transport mechanisms, Hester et al., 2017), bio-diffusion (in

93   which pore fluids and sediment are "pumped" through benthic macrofauna and plants,

94   Thibodeaux et al., 2011), and the streambed's permeability and porosity fields (which can

95   vary temporally and spatially, Laube et al., 2018; Newcomer et al., 2016; Stewardson et

96   al., 2016; Salehin et al., 2004; Herzog et al., 2018).

97   At present, only under highly idealized experimental or modeling conditions is it

98   possible to resolve the spatially and temporally complex eddy advection pathways

99   generated by the transport mechanisms described above. Due to its simplicity,

100   mathematical tractability and prior agreement with scaling studies, a common alternative

101   is to approximate mass transport across the SWI, and through the benthic biolayer, as a

102   flux-gradient diffusive process (Voermans et al., 2018):

103    $$J(y,t) = -D_{\text{eff}}(y)\frac{\partial(\theta C_s)}{\partial y}$$ (1a)

104   Here, $J(y,t)$ [M L^{-2} T^{-1}] and $C_s(y,t)$ [M L^{-3}] are the horizontally and temporally averaged

105   vertical flux and interstitial solute concentration at depth y [L] and time t [T] in the

106   sediment. The effective diffusivity, D_{eff} [L^2 T^{-1}], for solute mixing in the surficial

107   sediments of a stream or coastal sediment sums over contributions from the tortuosity-

108   modified molecular diffusion, D_m' [L^2 T^{-1}], dispersion, D_d [L^2 T^{-1}], and turbulent

109   diffusion, D_t [L^2 T^{-1}] (Roch et al., 2019; Roche et al., 2018; Grant et al., 2018b; Voermans

110   et al., 2018; Voermans et al.,2017; Chandler et al., 2016; Zhong et al., 2016; Boano et al.,

111   2014; Grant et al., 2012; Boano et al., 2011; Grant and Marusic, 2011; Reidenbach et al.,

112   2010; O'Connor and Harvey, 2008; O'Connor and Hondzo, 2008; Packman et al., 2004;

113   Nagaoka and Ohgaki, 1990; Richardson and Parr, 1988):

114    $D_{eff} = D'_m + D_d + D_t$ (1b)

115   Dispersion arises from spatial correlations between the time-averaged vertical velocity

116   component and the local mean solute concentration, while turbulent diffusion arises from

117   temporal correlations between the turbulent vertical velocity component and the

118   instantaneous turbulent concentration field (Voermans et al., 2018).

119   The use of equations (1a) and (1b) to describe mixing in the benthic biolayer

120   raises three questions. First, given that the mean flow and shear (turbulence) fields

121   responsible for mixing across the benthic biolayer are damped out with depth by viscous

122   dissipation (He et al., 2019; Roche et al, 2018; Voermans et al., 2017; Pokrajac and

123   Manes, 2009; Bruegem et al., 2006) how should the effective diffusivity be structured

124   vertically, and does the answer depend on the nature of the transport mechanism under

125   consideration (e.g., dispersion or turbulent diffusion)? Second, once an appropriate

126   vertical structure is selected for the effective diffusivity, how well does the flux-gradient

127   diffusive model (equation (1a)) represent solute transport through the streambed? Third,

128   how do we extrapolate effective diffusivities measured in the laboratory to streams and

129   coastal sediments? In this paper we focus on addressing these three questions in the

130   context of turbulent mixing across a flat sediment bed. Complementary efforts are

131   underway to address mixing in the benthic biolayer by bedform pumping and bedform

132   turnover.

133   The paper is organized as follows. In **Section 2** we demonstrate, through an

134   application of Duhamel's Theorem (Perez et al., 2013), that solute concentration in the

135   interstitial fluids of the sediment bed can be represented as the convolution of solute

136   concentration in the water column and a Green's function for mass transport in the

137   interstitial fluids of the streambed (Leij et al., 2000). This starting point leads to a set of

138   explicit solutions, valid for any Green's function, for the spatiotemporal evolution of

139   solute concentration in the water and sediment columns of a closed system. Notably,

140   these solutions capture the two-way coupling of evolving solute concentrations above and

141   below the SWI, whereby mass transfer out of the streambed alters mass concentration in

142   the overlying water column which, in turn, alters mass transfer into the streambed, and so

143   on (**Figure 1b**). We then derive six Green's functions for two choices of the lower

144   boundary condition (finite or semi-infinite sediment domain) and four functional forms of

145   the diffusivity depth profile. In **Section 3** we demonstrate how this theory can be used to

146   simulate unsteady mass transfer in a stirred tank experiment, and in **Section 4** apply it to

147   previously published measurements of turbulent mass transfer across a flat

148   unconsolidated sediment bed in a well-stirred tank (Chandler et al., 2016; Chandler,

149   2012). We address the three questions raised above in **Section 5** and present our

150   conclusions in **Section 6**.

151   [Figure 1 goes about here]

152   **2 Analytical Modeling Framework**

153   **2.1 Governing Equations for Turbulent Mixing in the Benthic Biolayer**

154   Double averaging over the turbulent timescale (e.g., estimated from the ratio of water

155   depth and stream velocity (Pope, 2012)) and the horizontal plane of the SWI, and

156   assuming that streambed porosity does not change appreciably through the benthic

157   biolayer (i.e., the variable θ appearing in equation (1a) is a fixed constant in the upper 5

158   cm or so of the streambed (Knapp et al., 2017)), we obtain the following mass

159   conservation equation for one-dimensional diffusion of a solute through the interstitial

160   fluids of the sediment bed:

161   $$\frac{\partial C_s}{\partial t} = \frac{\partial}{\partial y}\left(D_{\text{eff}}(y)\frac{\partial C_s}{\partial y}\right)$$ (2a)

162   Equation (2a) equates the accumulation of mass in a differential horizontal slice of the

163   sediment beneath a turbulent stream (left hand side) to the vertical diffusive transport

164   (right hand side) of a conservative (non-reactive and non-adsorbing) solute (Incropera et

165   al., 2007). The coordinate y increases with depth into the streambed and its origin (at

166   $y=0$) is positioned at the horizontal plane of the SWI (**Figure 1a**).

167   In this study we explore four functional forms of the effective diffusivity depth

168   profile, $D_{\text{eff}}(y) = D_{\text{eff},0}f(y)$, where the variable $D_{\text{eff},0}$ is the surficial effective diffusivity (at

169   the SWI, $y=0$) and $f(y)$ (unitless) is a piecewise continuous function that equals unity at

170   the SWI (i.e., $f(0)=1$). After substituting this functional form for the effective diffusivity,

171   equation (2a) can be rewritten in dimensionless form where the new dependent variable,

172   c_s [-], incorporates the solute's initial concentration in the interstitial pore fluids of the

173   sediment bed and the overlying water column (C_{s0} and C_{w0} [M L^{-3}], respectively):

174    $$\frac{\partial c_s}{\partial \bar{t}} = \frac{\partial}{\partial \bar{y}}\left(f(\bar{y})\frac{\partial c_s}{\partial \bar{y}} \right)$$ (2b)

175    $$c_s(\bar{y},\bar{t}) = \frac{C_s(\bar{y},\bar{t}) - C_{s0}}{C_{w0} - C_{s0}}, \ c_s(\bar{y},\bar{t}) \in [0,1]$$ (2c)

176    $$\bar{t} = t/t_{\mathrm{T}} \geq 0, \ t_{\mathrm{T}} = 1/\left(D_{\mathrm{eff},0}a^2\right), \ \bar{y} = ay \geq 0$$ (2d)

177   The constant a [L^{-1}] is an inverse depth-scale (the definition of which depends on the

178   choice of diffusivity profile, see later) and t_{T} is a time constant for solute mixing in the

179   benthic biolayer. Given the definition of the dimensionless concentration group (equation

180   (2c)), the initial condition for equation (2b) becomes:

181    $$c_s(\bar{y},\bar{t}=0) = 0$$ (3a)

182   At the upper boundary (at the SWI, $y=0$) we require that the interstitial tracer

183   concentration equals the tracer concentration in the overlying water column,

184    $C_s(y=0,t) = C_w(t)$ [M L^{-3}], which depends only on time; i.e., solute concentration in the

185   water column is well-mixed. Expressed in dimensionless form the upper boundary

186   condition becomes:

187    $$c_s(\bar{y}=0,\bar{t}) = \frac{C_w(\bar{t}) - C_{s0}}{C_{w0} - C_{s0}}H(\bar{t}) = c_w(\bar{t})H(\bar{t})$$ (3b)

188    $$c_w(\bar{t}) = \frac{C_w(\bar{t}) - C_{s0}}{C_{w0} - C_{s0}}, \ c_w(\bar{t}) \in [0,1], \ H(\bar{t}) = \begin{cases} 0, \ \bar{t} < 0 \\ 1, \ \bar{t} > 0 \end{cases}$$ (3c)

189   The Heaviside function $H(\bar{t})$ [-] appearing on the righthand side of equation (3b) ensures

190   that the upper boundary condition is zero for $\bar{t} < 0$ (this detail becomes important for the

191   application of Duhamel's Theorem below). By expressing the upper boundary condition

192   in this way, we are assuming that mass transfer across the SWI is rate-limited by the

193   mixing of solute within the streambed and not by convective mixing across the

194   concentration boundary layer above the streambed (Grant et al., 2018). Put another way,

195   we are assuming that the Biot Number—which expresses the ratio of timescales for

196   diffusive mixing in the streambed and convective mass transfer across the turbulent

197   boundary layer above the streambed—is much greater than unity (Incropera et al., 2007).

198   One of two lower boundary conditions can be selected, depending on whether the

199   sediment bed is assumed to be finite (equation (3d)) or semi-infinite (equation (3e)) in

200   extent.

201     $\left. \dfrac{\partial c_s}{\partial \overline{y}} \right|_{\overline{y}=\overline{d}_b} = 0$ (3d)

202     $c_s\left(\overline{y}\to\infty,\overline{t}\right)=0$ (3e)

203   Equation (3d) enforces a no-flux boundary condition at scaled depth $\overline{d}_b = a\,d_b$ [-] where d_b

204   [L] is the depth of the sediment bed (**Figure 1**). Equation (3e) implies that, very deep into

205   the bed ($\overline{y}\to\infty$), the interstitial concentration is maintained at its initial state.

206   **2.2 Duhamel's Theorem and Green's Functions**

207   We seek an explicit solution to the above system of equations that is valid for any time-

208   varying solute concentration in the overlying water column, any piecewise continuous

209   diffusivity profile, and either a finite or semi-infinite streambed. To this end we invoke

210   Duhamel's Theorem, an analytical approach for solving the diffusion equation in cases

211   where one boundary is a piece-wise continuous function of time (Perez Guerrero et al.,

212   2013). Proofs of this theorem typically assume that the diffusion coefficient is constant.

213   However, as demonstrated in the Supplemental Information (**Text S1**), the theorem also

214   applies in cases where the diffusion coefficient varies solely as a function of depth.

215   For the version of Duhamel's Theorem adopted here, three conditions must be

216   met (Myers, 1971): (1) the system must have a zero initial state; (2) the differential

217   equation and boundary conditions must be homogeneous with the exception of a single

218   time-dependent boundary condition or source/sink term in the differential equation; and

219   (3) the single nonhomogeneous term should be initially equal to zero. By design, our

220   system meets all three requirements. Accordingly, Duhamel's Theorem allows us to

221   express the interstitial solute concentration in the sediment bed as a convolution of the

222   time-derivative of the water column concentration $c_w(\bar{t})$ and a so-called *auxiliary*

223   *function* $c_s^A(\bar{y},\bar{t})$ where v is a dummy integration variable (Meyers, 1971):

224    $$c_s(\bar{y},\bar{t})=\int_0^{\bar{t}} c_s^A(\bar{y},\bar{t}-v)\frac{d}{dv}\big[c_w(v)H(v)\big]dv \qquad\qquad\text{(4a)}$$

225   The auxiliary function is, by definition, a solution to the same system of equations

226   described above for the interstitial solute concentration (equations (2b) - (3e)) but with

227   the nonhomogeneous term replaced by unity (compare equations (3b) and (4d)):

228    $$\frac{\partial c_s^A}{\partial \bar{t}}=\frac{\partial}{\partial \bar{y}}\left(f(\bar{y})\frac{\partial c_s^A}{\partial \bar{y}}\right) \qquad\qquad\text{(4b)}$$

229    $$c_s^A(\bar{y},\bar{t}=0)=0,\ \bar{y}\geq 0 \qquad\qquad\text{(4c)}$$

230    $$c_s^A(\bar{y}=0,\bar{t})=H(\bar{t}) \qquad\qquad\text{(4d)}$$

231   The auxiliary function's lower boundary condition depends on whether the sediment bed

232   is finite or semi-infinite in extent:

233    $$\left.\frac{\partial c_s^A}{\partial \bar{y}}\right|_{\bar{y}=\bar{d}_b,\bar{t}}=0 \qquad\qquad\text{(4e)}$$

234    $$c_s^A(\bar{y}\rightarrow\infty,\bar{t})=0 \qquad\qquad\text{(4f)}$$

235 Duhamel's Theorem (equation (4a)) can also be expressed as a convolution of the

236 dimensionless water column concentration, $c_w(\bar{t})$, and a so-called Green's function,

237 $G(\bar{y},\bar{t})$ [T^{-1}], scaled here by the mixing timescale introduced earlier, $\bar{G}(\bar{y},\bar{t})=t_\mathrm{T}G(\bar{y},\bar{t})$ (see

238 **Text S2** for details):

$$c_s(\bar{y},\bar{t})=\int_0^{\bar{t}}\bar{G}(\bar{y},v)c_w(\bar{t}-v)dv \qquad (5a)$$

$$\bar{G}(\bar{y},\bar{t})=\frac{\partial c_s^A}{\partial \bar{t}} \qquad (5b)$$

241 According to equation (5a), solute concentration in the interstitial fluid of the sediment

242 bed at any depth and time, $c_s(\bar{y},\bar{t})$, depends on the entire prior history of solute

243 concentration in the water column, $c_w(\bar{t})$, filtered through the Green's function, $\bar{G}(\bar{y},\bar{t})$.

244 The Green's function, in turn, is a fundamental solution to the diffusion equation

245 (equation (2b)) that characterizes the response of solute concentration in the interstitial

246 fluids of the streambed to an impulsive injection of mass at the SWI at $\bar{t}=0$, $c_w(\bar{t})=\delta(\bar{t})$,

247 where $\delta(\bar{t})$ [-] is the Dirac Delta function. Because the Green's function is calculated

248 from the auxiliary function (equation (5b)) its functional form will depend on the vertical

249 structure of the diffusivity profile, $f(\bar{y})$, and the lower boundary condition (either

250 equation (4e) or (4f)). Five Green's functions, corresponding to different combinations of

251 the diffusivity profile and lower-boundary condition, are derived in **Section 2.4**.

252 **2.3 Two-Way Coupling Across the SWI in a Closed System**

253 In a typical application of Duhamel's Theorem, the time-dependence of the

254 nonhomogeneous boundary condition is stipulated in advance. In our case, however, the

255   nonhomogeneous boundary condition (i.e., the water column concentration, equation

256   (3b)) depends on mass flux across the SWI through a mass balance over the water

257   column. For a closed system with a well-mixed water column, such as the stirred tank in

258   **Figure 1b**, the water column mass balance takes on the following form:

259     $$A_b h_w \frac{dC_w}{dt} = A_b \theta D_{eff,0} \frac{\partial C_s}{\partial y}\Big|_{y=0,t} \qquad (6a)$$

260   In this equation, the change of solute mass in the water column (left hand side) equals the

261   rate of mass transfer across the SWI by turbulent mixing (right hand side). New variables

262   appearing here include the interfacial area, A_b [L^2], of the streambed and the height of the

263   water column, h_w [L]. Streambed porosity, θ, is included on the right-hand side of the

264   equation to account for the streambed's porosity; specifically, the abrupt change in area

265   over which solute mass transport occurs above and below the SWI (Grant et al., 2012).

266   Expressing equation (6a) using the dimensionless variables introduced earlier, we obtain

267   equation (6b) where the dimensionless variable, $\bar{h}_w$ (equation (6c)), is a scaled form of

268   the water column depth.

269     $$\frac{dc_w}{d\bar{t}} = \frac{1}{\bar{h}_w} \frac{\partial c_s}{\partial \bar{y}}\Big|_{\bar{y}=0,\bar{t}} \qquad (6b)$$

270     $$\bar{h}_w = \frac{a h_w}{\theta} \qquad (6c)$$

271   Two-way coupling across the SWI manifests mathematically as a dependence of

272   the water column concentration (left hand side, equation (6b)) on the streambed's

273   interstitial solute concentration (right hand side, equation (6b)) and, simultaneously, the

274   dependence of the streambed's interstitial solute concentration (left hand side, equation

275   (5a)) on the solute concentration in the water column (through its convolution with the

276   Green's function, right hand side equation (5a)). This two-way coupling can be solved

277   exactly by manipulating the water and sediment mass balance equations in the Laplace

278   Domain. As demonstrated in Supplemental Information (**Text S3**), the result is a set of

279   fully coupled solutions for solute concentration in the water and sediment columns of a

280   closed system with two-way coupling across the SWI "turned on":

281    $$C_w(\bar{t}) = (C_{w0} - C_{s0})\mathcal{L}^{-1}\left[\frac{1/\bar{s}}{1 - \frac{1}{\bar{s}\bar{h}_w}(\partial\tilde{G}/\partial\bar{y})_{\bar{y}=0,\bar{s}}}\right] + C_{s0} \tag{7a}$$

282    $$C_s(\bar{y},\bar{t}) = (C_{w0} - C_{s0})\mathcal{L}^{-1}\left[\frac{\tilde{G}(\bar{y},\bar{s})/\bar{s}}{1 - \frac{1}{\bar{s}\bar{h}_w}(\partial\tilde{G}/\partial\bar{y})_{\bar{y}=0,\bar{s}}}\right] + C_{s0} \tag{7b}$$

283   In these solutions, the symbol $\mathcal{L}^{-1}[\cdot]$ represents the inverse Laplace Transform, $\bar{s} = st_T$ [-]

284   is a dimensionless form of the Laplace Transform variable s [T⁻¹], and $\tilde{G}$ is the Laplace

285   transform of the dimensionless Green's function which, in turn, depends on the

286   diffusivity depth profile $f(\bar{y})$ and bottom boundary condition (through the solution to the

287   auxiliary function (equation (5b)). A corresponding set of solutions can also be derived

288   for when two-way coupling across the SWI is "turned off"; i.e., the diffusion equation's

289   upper boundary condition is held at its initial state, $C_s(\bar{y}=0,\bar{t}) = C_{w0}$:

290    $$C_w(\bar{t}) = (C_{w0} - C_{s0})\mathcal{L}^{-1}\left[\frac{1}{\bar{s}}\left(\frac{1}{\bar{s}\bar{h}_w}\frac{\partial\tilde{G}}{\partial\bar{y}}\bigg|_{\bar{y}=0,\bar{s}} + 1\right)\right] + C_{s0} \tag{7c}$$

291    $$C_s(\bar{y},\bar{t}) = (C_{w0} - C_{s0})\mathcal{L}^{-1}\left[\frac{\tilde{G}(\bar{y},\bar{s})}{\bar{s}}\right] + C_{s0} \tag{7d}$$

292   [Figure 2 goes about here]

293 Depending on the choice of Green's function, the inverse Laplace transforms appearing

294 in equations (7a) - (7d) were either determined analytically, or numerically evaluated

295 using Gaussian Quadrature implemented in the Mathematica package authored by U.

296 Graf (Graf, 2004).

297 **2.4 Laplace Domain Solutions for the Green's Function**

298 In **Table 1** we present five Laplace domain solutions for the Green's function given four

299 different choices of the diffusivity depth profile and two different choices of the bottom

300 boundary condition (finite or semi-infinite sediment bed) (derivations in Supplemental

301 Information**, Text S4)**. Together with equations (7a) through (7d), these five Green's

302 functions provide a total of 20 different solution combinations for solute concentration in

303 the water and sediment column of a closed system with two-way coupling across the SWI

304 turned on (equations (7a) and (7b)) or off (equations (7c) and (7d)). The four diffusivity

305 depth profiles we evaluated include (**Figure 2**): (1) constant (*C Profile*, equation (8a));

306 (2) exponentially declining (*E Profile*, equation (8b)); (3) exponentially declining to a

307 tortuosity-modified molecular diffusion coefficient (*E2M Profile*, equation (8c)); and (4)

308 constant to exponentially declining diffusivity (*C2E Profile*, equation (8d)).

309 $f_{\mathrm{C}}(\bar{y})=1$, $\bar{y}=a_{\mathrm{C}}y$ (8a)

310 $f_{\mathrm{E}}(\bar{y})=e^{-\bar{y}}$, $\bar{y}=a_{\mathrm{E}}y$ (8b)

311 $f_{\mathrm{E2M}}(\bar{y})=\begin{cases} e^{-\bar{y}},\, 0\leq\bar{y}\leq\bar{\ell}_{m} \\ \bar{D}=D'_{\mathrm{m}}/D^{\mathrm{E2M}}_{\mathrm{eff},0},\, \bar{y}>\bar{\ell}_{m} \end{cases}$, $\bar{\ell}_{m}=-\ln\bar{D}$, $0<\bar{D}<1$, $\bar{y}=a_{\mathrm{E2M}}y$ (8c)

312 $f_{\mathrm{C2E}}(\bar{y})=\begin{cases} 1,\, 0\leq\bar{y}\leq\bar{\ell}_{t} \\ e^{-(\bar{y}-\bar{\ell}_{t})},\, \bar{y}>\bar{\ell}_{t} \end{cases}$, $\bar{\ell}_{t}=a_{\mathrm{C2E}}\ell_{t}$, $\bar{y}=a_{\mathrm{C2E}}y$ (8d)

313   Most laboratory (Marion and Zaramella, 2015; O'Connor and Harvey, 2008; Grant et al.,

314   2012) and field (Wörman, 2000) studies of diffusive mixing across the SWI adopt the C

315   Profile. However, several studies (He et al., 2019; Roche et. al, 2019; Chandler et al.,

316   2016; Nagaoka and Ohgaki, 1990) have shown that turbulent mixing in the sediment bed

317   declines exponentially with depth, and a recent numerical modeling study concluded that

318   the E Profile is consistent with experimental breakthrough curves measured in the

319   laboratory and field (Bottacin-Busolin, 2019). The E2M profile is a natural extension of

320   the E Profile that accounts for the fact that the tortuosity-modified molecular diffusion

321   coefficient D'_m [L^2 T^{-1}] imposes a lower-bound on the effective diffusivity. E2M's

322   mathematical representation (equation (8c)) includes two new variables: the

323   dimensionless depth at which the diffusivity profile transitions from exponentially

324   declining to the tortuosity-modified molecular diffusion coefficient, $\overline{\ell}_m = a_{E2M}\ell_m$ [-] where

325   ℓ_m [L] is the transition depth and $\overline{D} = D'_m / D^{E2M}_{eff,0}$ [-] is a dimensionless form of the

326   tortuosity-modified molecular diffusion coefficient. These two parameters are

327   mathematically related as follows: $\overline{\ell}_m = -\ln\overline{D}$. Finally, the C2E Profile captures enhanced

328   mixing at the top of the streambed by extending the surficial effective diffusivity $D^{C2E}_{eff,0}$ to

329   a depth $y = \ell_t$ [L] below the SWI. For depths greater than the constant mixing thickness,

330    $y > \ell_t$, the diffusivity profile declines exponentially. The dimensionless form of the

331   enhanced mixing thickness ℓ_t is defined in the usual way, $\overline{\ell}_t = a_{C2E}\ell_t$.

332   [Table 1 goes about here]

333   **3 Example of the Theory's Application to Mixing Across the SWI in a Stirred Tank**

334   As a tangible example of the theory presented in **Section 2**, consider an experiment

335   (along the lines examined in detail later, see **Section 4**) in which a mass M of a

336   conservative solute is added to the interstitial fluids of a sediment bed in an otherwise

337   solute-free stirred tank. Adopting the notation indicated in **Figure 1b**, the initial

338   interstitial solute concentration in the sediment bed will be: $C_{s0} = M/(d_b A_b \theta)$. At time $t=0$

339   the impeller is turned on causing solute concentration in the overlying water column to

340   increase as solute turbulently mixes out of the bed. If the experiment runs long enough,

341   the solute concentration in the water column and interstitial fluids of the sediment bed

342   will approach a final (well-mixed) equilibrium concentration, C_{eq} [M L^{-3}]:

343
$$\frac{C_{eq}}{C_{s0}} = \frac{\bar{d}_b}{1+\bar{d}_b}, \quad \bar{d}_b = d_b \theta / h_w \qquad \qquad (9a)$$

344   How does solute concentration in the overlying water column and interstitial fluids of the

345   sediment bed evolve from their initial state (where all solute mass is located in the

346   sediment bed) to the final (well-mixed) state given by equation (9a)? Within the context

347   of our modeling framework, the answer depends on the depth-dependence of the

348   diffusivity profile, whether two-way coupling across the SWI is turned "on" or "off", and

349   whether the sediment bed is assumed to be semi-infinite or finite in extent.

350   As an illustration we adopt the C Profile and derive from the theoretical

351   framework in **Section 2** the following three explicit solutions for the evolution of solute

352   concentration in the water column (see **Text S5** for details): (1) a "null model" which

353   assumes two-way coupling across the SWI is turned off and the sediment bed is infinitely

354   deep (equation (9b)); (2) an "infinite bed" model that assumes two-way coupling is

355   turned on and the sediment bed is infinitely deep (equation (9c)); and (3) a "finite bed"

356   model that accounts for both two-way coupling across the SWI and the finite depth of the

357   sediment bed (equation (9d)).

358
$$\frac{C_{w,null}^{C}(\bar{t}_C)}{C_{s0}} = 2\sqrt{\frac{\bar{t}_C}{\pi}} \ , \ \bar{t}_C = \theta^2 D_{eff,0}^{C} t / h_w^2 \tag{9b}$$

359
$$\frac{C_{w,\infty}^{C}(\bar{t}_C)}{C_{s0}} = 1 - e^{\bar{t}_C} \mathrm{erfc}\left(\sqrt{\bar{t}_C}\right) \tag{9c}$$

360
$$\frac{C_{w,finite}^{C}(\bar{t}_C)}{C_{s0}} = 1 - \mathcal{L}^{-1}\left[\frac{1/\bar{s}}{1 + \tanh\left(\bar{d}_b\sqrt{\bar{s}}\right)/\sqrt{\bar{s}}}\right] \tag{9d}$$

361   The corresponding set of solutions for solute concentration in the interstitial fluids of the

362   sediment bed are as follows:

363
$$\frac{C_{s,null}^{C}(\bar{y}_C, \bar{t}_C)}{C_{s0}} = \mathrm{erfc}\left(\frac{\bar{y}_C}{\sqrt{4\bar{t}_C}}\right) \ , \ \bar{y}_C = \theta y / h_w \tag{10a}$$

364
$$\frac{C_{s,\infty}^{C}(\bar{y}_C, \bar{t}_C)}{C_{s0}} = 1 - e^{\bar{t}_C + \bar{y}_C} \mathrm{erfc}\left(\frac{2\bar{t}_C + \bar{y}_C}{\sqrt{4\bar{t}_C}}\right) \tag{10b}$$

365
$$\frac{C_{s,finite}^{C}(\bar{y}_C, \bar{t}_C)}{C_{s0}} = 1 - \mathcal{L}^{-1}\left[\frac{\cosh\left((\bar{d}_b - \bar{y}_C)\sqrt{\bar{s}}\right)}{\bar{s}\cosh\left(\bar{d}_b\sqrt{\bar{s}}\right) + \sqrt{\bar{s}}\sinh\left(\bar{d}_b\sqrt{\bar{s}}\right)}\right] \tag{10c}$$

366   The superscript "C" indicates that these solutions are specific to the C Profile.

367   The null model predicts that solute concentration in the water column increases

368   without bound and in proportion to the square root of time (i.e., solute concentration in

369   the water column increases linearly when plotted against $\sqrt{\bar{t}_C}$, thick black dashed line,

370   **Figure 3a**). The infinite bed model rises with the null model initially (i.e., until around

371     $\sqrt{\bar{t}_C} \approx 0.25$) but then slows as two-way coupling reduces the rate of mass transfer across

372   the SWI (thin black solid curve in **Figure 3a**). The finite bed model exhibits three phases

373   (colored dashed lines in the figure): tracking the null solution early on, transitioning to

374   the infinite bed solution at intermediate times, and stabilizing at a final equilibrium

375   concentration at long times (thin horizontal colored lines).

376   [Figure 3 goes about here]

377   Similar patterns are evident for model-predicted solute concentration in the

378   interstitial fluids of the streambed (**Figure 3b**). For these simulations we focused on the

379   temporal evolution of interstitial solute concentration in the shallow portion of the bed,

380 $\bar{y}_c = 0.05$; this particular depth was chosen so that we would not violate the inequality

381   requirement, $\bar{y}_c \leq \bar{d}_b$, for the smallest dimensionless bed depth of $\bar{d}_b = 0.1$ (light blue

382   horizontal lines in **Figure 3**). The null model (thick black dashed curve) predicts a steep

383   drop in solute concentration initially (as solute in the upper portion of the streambed

384   mixes into a solute-free water column) followed by a gradual decline with time (as solute

385   from deeper in the bed mixes upward). The infinite bed solution (thin black curve)

386   declines with the null model initially, but then rebounds as two-way coupling slows mass

387   transfer across the SWI. Indeed, this rebound closely approximates the rise in water

388   column concentration predicted by the infinite bed model (compare thin black curves in

389   **Figures 3a** and **3b**) implying that, when two-way feedback is turned on, solute

390   concentrations in the interstitial fluids near the top of the sediment bed are similar to the

391   solute concentration in the overlying water column. Interstitial solute concentrations

392   predicted by the finite bed model (colored dashed curves in **Figure 3b**) exhibit the same

393   three phases noted above for the water column; namely, they track the null model at early

394   times, follow the infinite bed model at intermediate times, and stabilize at an equilibrium

395   concentration at long times. For the model-data comparisons described in the next section

396   we employ a set of infinite bed models derived for each of the four diffusivity profiles (C,

397   E, E2M, and C2E) and restrict the experimental time window to well before the onset of

398   equilibrium conditions.

399   **4 Applying the Theory to Previously Published Measurements**

400   **4.1 Chandler et al.'s Experiments**

401   Next we turn to an extensive set of previously published measurements of turbulent

402   mixing of a conservative tracer (Rhodamine WT) across the SWI in a stirred tank with a

403   flat sediment bed, along the lines of the experimental set-up illustrated in **Figure 1b**

404   (Chandler et al., 2016; Chandler, 2012). Chandler et al.'s study is notable for several

405   reasons. First, it is one of the few where tracer concentrations were simultaneously

406   measured in the water and sediment columns allowing us to directly compare mixing

407   parameters estimated from data collected exclusively above or below the SWI. Second,

408   the twenty (out of twenty-six total) Chandler et al. experiments included in this study

409   cover a range of bed shear velocities ($u_* = $ 0.01 to 0.04 m s^{-1}), mean grain diameters ($d_g = $

410   0.15 to 5.00 mm), and sediment permeabilities ($K = $ 0.18 to 223 m^2). Finally, by

411   conceptually dividing the sediment bed into a series of layers and fitting the diffusion

412   equation (with a constant diffusivity profile) to each layer separately, Chandler et al.

413   concluded that the diffusivity declines exponentially with depth. Nagaoka and Ohgaki

414   (1990), who pioneered this approach, reached a similar conclusion. Thus, there is already

415   a strong indication that the diffusivity in their system declines with depth. One caveat is

416   that Chandler et al.'s range of shear velocities is on the low side for some streams; e.g.,

417   the 72 headwater streams included in the U.S. Lotic Intersite Nitrogen eXperiment (LINX

418   II) had shear velocities ranging from 0.02 to 0.48 m s^{-1} and only seven streams had shear

419   velocities in the range interrogated by Chandler et al. (Hall et al., 2009). However, when

420   the shear velocity and permeability for each of Chandler et al.'s experiments are

421   combined to calculate a Permeability Reynolds Number, this master variable spans both

422   dispersive and turbulent diffusive mixing regimes (see **Section 5.1**).

423   Details of Chandler et al.'s experiments and the approach we used for parameter

424   estimation and model performance evaluation are briefly described here (see **Text S6** for

425   details). In brief, the sediment column, which had a depth of $d_b = 0.2$ m and a porosity of

426    $\theta =$ 0.38 to 0.39, consisted of randomly packed single-sized spherical soda glass spheres.

427   In all experiments, the initial state was a Rhodamine WT saturated sediment bed

428   (concentration of $C_{s0} = 100$ ppb) and a Rhodamine-free water column ($C_{w0} =$ 0 ppb)

429   although the actual concentrations varied somewhat by experiment (**Table S1**).

430   Experiments were initiated when the impeller motor was turned on, whereupon tracer

431   concentrations were fluorometrically monitored in the water column and at 5 depths in

432   the sediment column ($x =$ 0.015, 0.049, 0.083, 0.117, and 0.151 m below the SWI) at a

433   frequency of 0.1 Hz over a period of hours to days. Diffusivity profile parameters were

434   inferred by minimizing the root mean squared error (RMSE) calculated from

435   observations and profile-specific infinite bed model predictions using the non-linear least

436   squares algorithms implemented within the "NonlinearModelFit" command in the

437   Mathematica computing package (v. 11.20, Wolfram Research, Inc.). Several model

438   performance metrics were also generated, including RMSE, coefficient of determination

439   (R^2 value), and the corrected Akaike Information Criterion (AICc). The latter was used to

440   rank the performance of the four diffusivity profile models, accounting for the trade-off

441   between model fit and model complexity. The top-ranked (most parsimonious) model has

442   the smallest AICc value (Aho et al., 2014). Because model predictions were based on

443   "infinite bed models" specific to each profile (see **Section 3**), we restricted the

444   experimental window to periods when the bottom interstitial Rhodamine WT

445   concentration, as measured by the deepest probe, was within 90% of its initial value (see

446   t_{final} values in **Table S1**). By this approach, diffusivity profile parameters were estimated

447   for all four diffusivity profiles (C, E, E2M, and C2E) and for 20 of Chandler et al.'s

448   experiments (inferred parameter values, estimated errors, and model performance metrics

449   are summarized in **Tables S2-S7**); six experiments were excluded due to missing data or

450   other issues.

451   **4.2 Experimental Evaluation of the C Profile**

452   Significant bias is evident when tracer concentrations predicted by the C Profile's infinite

453   bed model are compared to Chandler et al.'s experimental data (**Figure 4a**). In this figure

454   we have plotted Chandler et al.'s Rhodamine WT measurements against the square root

455   of dimensionless time, $\sqrt{\bar{t}_C} = \sqrt{t/t_C}$, where the time-constant, $t_C = h_w^2 \big/ \left(\theta^2 D_{eff,0}^C \right)$, varies from

456   experiment-to-experiment depending on the inferred value of the C Profile's effective

457   diffusivity (summarized in **Table S2**); the other two parameters, h_w and θ, varied little

458   across Chandler et al.'s twenty experiments. When plotted in this way Chandler et al.'s

459   data can be compared directly to a single model-predicted curve for the time evolution of

460   Rhodamine WT concentration in the water column (solid black curve, equation (9c), top

461   panel in **Figure 4a**) and at two depths (15 or 151 mm below the SWI) in the sediment

462   column (solid black curves, equation (10b), bottom panel in **Figure 4a**). For clarity,

463   Rhodamine WT measurements at the three intermediate depths (4.9, 8.3, and 117 cm

464   below the SWI) were not included this figure, although these data were included in the

465   model optimization studies described in **Section 5.1**.

466   [Figure 4 goes about here]

467   By virtue of the way Chandler et al.'s experiments were conducted, the

468   Rhodamine WT concentration in the water column is proportional to the cumulative

469   Rhodamine WT mass transferred from the sediment bed to the water column over time.

470   The results plotted in the top panel of **Figure 4a** therefore imply that the C Profile model

471   under- and over-estimates mass transfer out of the sediment bed at short and long times,

472   respectively. A comparison of model-predicted and measured Rhodamine WT

473   concentrations in the sediment bed reveals the problem (bottom panel, **Figure 4a**): the C

474   Profile model under-estimates mixing in the surficial portion of the bed at early times

475   (i.e., predicted concentrations exceed measured concentrations at 15 mm below the SWI)

476   and over-estimates mixing deeper in the bed at later times (i.e., predicted concentrations

477   are less than measured concentrations at 151 mm below the SWI).

478   **4.3 Experimental Evaluation of the E Profile**

479   The model bias described above is reduced substantially when the effective diffusivity

480   decays exponentially with depth (**Figure 4b**). The E Profile's infinite bed model was

481   constructed by substituting its Green's function (equation (T3)) into the water and

482   sediment mass balance solutions (equations (7a) and (7b)) for a closed system with two-

483   way coupling across the SWI "turned on" (the superscript "E" indicates that these

484   solutions are specific to the E Profile):

485    $$C_{w,\infty}^{E}\left(\bar{t}_{E}\right)=\left(C_{w0}-C_{s0}\right)\mathcal{L}^{-1}\left[\frac{\bar{h}_{w}K_{1}\left(2\sqrt{s}\right)}{s\bar{h}_{w}K_{1}\left(2\sqrt{s}\right)+\sqrt{s}K_{0}\left(2\sqrt{s}\right)}\right]+C_{s0} \qquad (11a)$$

$$486 \quad C_{s,\infty}^{E}\left(\bar{y},\bar{t}_{E}\right)=\left(C_{w0}-C_{s0}\right)\mathcal{L}^{-1}\left[\frac{\bar{h}_{w}\sqrt{e^{\bar{y}}}K_{1}\left(2\sqrt{e^{\bar{y}}s}\right)}{s\bar{h}_{w}K_{1}\left(2\sqrt{s}\right)+\sqrt{s}K_{0}\left(2\sqrt{s}\right)}\right]+C_{s0} \tag{11b}$$

$$487 \quad \bar{t}_{E}=t/t_{E}\ ,\ \ t_{E}=1/\left(a_{E}^{2}D_{eff,0}^{E}\right),\ \ \bar{h}_{w}=a_{E}h_{w}/\theta\ ,\ \ \bar{y}=a_{E}y \tag{11c}$$

488   Because the E Profile model has two unknown parameters ($D_{eff,0}^{E}$ and a_{E}, as opposed to the

489   C Profile's one unknown parameter, $D_{eff,0}^{C}$) there is no longer a single "master" curve

490   against which all of Chandler et al.'s water column data, for example, can be compared to

491   (as there was for the C Profile in the top panel of **Figure 4a**). Instead, for the E Profile

492   (and the C2E Profile described below) model-data comparisons must be conducted on an

493   experiment-by-experiment basis. In **Figure 4b** we therefore focus our model-data

494   comparison on a typical experiment (red symbols in the figure, experiment ID

495   #20110613). To generate model predictions for this experiment we: (1) fit equation (11a)

496   to the experiment's water column data yielding estimates for the inverse depth-scale and

497   effective diffusivity ($a_{E}=50\pm1.2$ m^{-1} and $D_{eff,0}^{E}=\left(5.6\pm0.5\right)\times10^{-6}$ m^{2} s^{-1}); and (2) plotted the

498   model against the same abscissa used in **Figure 4a** after applying the following

499   dimensionless time transformation, $\bar{t}_{E}=\left(\bar{h}_{w}^{2}D_{eff,0}^{E}/D_{eff,0}^{C}\right)\bar{t}_{C}$, and substituting experiment-

500   specific values for the dimensionless water depth ($\bar{h}_{w}=a_{E}h_{w}/\theta=33\pm14$) and the C Profile's

501   effective diffusivity ($D_{eff,0}^{C}=\left(3.4\pm0.2\right)\times10^{-7}$ m^{2} s^{-1}). Equation (11a) closely reproduces the

502   experiment's water column concentrations of Rhodamine WT (compare solid curve and

503   red points in **Figure 4b**, top panel), although some model bias is evident for $\sqrt{\bar{t}_{C}}<0.05$.

504   The E Profile's infinite bed model (equation (11b)) also captures the fast and slow mixing

505   of Rhodamine WT out of the shallow and deep portions of the sediment bed (compare

506   black curves and red points, lower panel, **Figure 4b**). The last result is notable given that

507   the parameter values used to generate these predictions were inferred from the water

508   column data; i.e., by fitting the E Profile's infinite bed model to measurements of

509   Rhodamine WT in the water column we can predict the evolution of Rhodamine WT in

510   the interstitial fluids of the sediment bed with reasonable fidelity.

511   **4.4 Experimental Evaluation of the E2M Profile**

512   Setting the tortuosity-modified molecular diffusion coefficient, D'_m, as a lower bound on

513   the effective diffusivity does not improve the E Profile's model performance. We arrived

514   at this conclusion by estimating a tortuosity-modified diffusion coefficient for Chandler

515   et al.'s experiments ($D'_m = 1.31 \times 10^{-10}$ m²s⁻¹) from the ratio of the molecular diffusion

516   coefficient for Rhodamine in water at 21°C ($D_m = 2.9 \times 10^{-10}$ m²s⁻¹) (Chandler 2012) and

517   the tortuosity of the sediment bed ($\tau = 2.22$), estimated by substituting the measured bed

518   porosity ($\theta = 0.39$) into an empirical formula proposed by Iversen and Jorgensen (1992)

519   for sandy beds: $\tau = 1 + 2(1-\theta)$. Values of the inverse depth-scale and effective diffusivity,

520   a_{E2M} and $D^{E2M}_{eff,0}$, were then inferred by fitting the E2M Profile's infinite bed model

521   (constructed by substituting equations (T5a,b,c) in **Table 1** into equations (7a) and (7b))

522   to Chandler et al.'s water column Rhodamine WT measurements. Repeating this process

523   for all twenty of Chandler et al.'s experiments reveals that the E2M's inverse depth-

524   scales and effective diffusivities are nearly identical to those inferred from the E Profile

525   model (**Figure S1**, also compare **Tables S4** and **S6**), implying that these two profiles are

526   functionally equivalent. This result can be rationalized by noting that the timescale for

527   mixing through the sediment column by molecular diffusion ($t_m = \ell^2_m / D'_m \approx 11$ months,

25

528   where the mixing depth is $\ell_m = -\ln\left(D'_m / D^{E2M}_{eff,0}\right)/a_{E2M}$, see equation (8c) and discussion

529   thereof) is much longer than the time period Chandler et al. conducted their experiments

530   (days to weeks). While the E2M Profile did not add value (relative to the E Profile) to our

531   analysis of Chandler et al.'s experiments, it might prove useful in settings with very low

532   levels of turbulence and relatively impermeable sediments (i.e., very small values of the

533   Permeability Reynolds Number, see **Section 5**).

534   **4.5 Experimental Evaluation of the C2E Profile**

535   The C2E Profile's infinite bed model provides a near perfect representation of Chandler

536   et al.'s water column data (**Figure 4c**). The C2E's infinite bed model was constructed by

537   substituting its Green's function (equations (T6a) - (T6c) in **Table 1**) into equations (7a)

538   and (7b). We then followed the same two-step procedure outlined in **Section 3.3**, by (1)

539   fitting the model to Rhodamine concentrations measured in the water column during Exp

540   ID# 20110613 ($D^{C2E}_{eff,0} = (1.5\pm0.07)\times10^{-6}\,\mathrm{m^2\,s^{-1}}$, $\ell_t = 0.04\pm0.002$ m, $a_{C2E} = 66\pm3.1\,\mathrm{m^{-1}}$); and

541   (2) plotting the model against the same abscissa used in **Figures 4a,b** after applying the

542   following dimensionless time transformation, $\bar{t}_{C2E} = \left(\bar{h}_w^2 D^{C2E}_{eff,0} / D^C_{eff,0}\right)\bar{t}_C$, and substituting

543   experiment-specific values for the dimensionless water depth ($\bar{h}_w = a_{C2E} h_w / \theta = 44\pm19$) and

544   the C Profile's effective diffusivity ($D^C_{eff,0} = (3.4\pm0.2)\times10^{-7}\,\mathrm{m^2\,s^{-1}}$). As noted above, the

545   C2E Profile's infinite bed model provides a near perfect match to Rhodamine WT

546   concentrations measured in the water column (compare solid curve and red points in

547   **Figure 4c**). However, when these same parameter values are used to estimate Rhodamine

548   WT concentration in the interstitial fluids of the bed, there is some loss of model

549   performance compared to the E Profile; i.e., the C2E model systematically

550   underestimates mixing in the streambed, especially for Rhodamine measurements at 15

551   mm below the SWI (compare lower panels in **Figures 4b** and **4c**).

552   **5. Discussion**

553   Here we expand our focus to include all twenty of Chandler et al.'s experiments with the

554   goal of answering the three questions raised in **Section 1**.

555   **5.1 How is the Effective Diffusivity Structured Vertically?**

556   From refractive index matched particle image velocimetry (RIM-PIV) studies of

557   turbulent motions across the SWI of a permeable streambed, Voermans et al. (2017)

558   concluded that the flux of mass and momentum is dominated by different transport

559   mechanisms (molecular diffusion, dispersion, turbulent diffusion) depending on the

560   magnitude of the Permeability Reynolds Number, $\mathrm{Re}_K = u_* \sqrt{K}/\upsilon$, a dimensionless

561   arrangement of the shear velocity u_* [L T^{-1}], sediment bed permeability K [L^2], and

562   kinematic viscosity of water υ [L^2 T^{-1}]. Specifically, molecular diffusion dominates

563   mixing across the SWI for small values of this dimensionless number ($\mathrm{Re}_K < 0.01$),

564   dispersion for intermediate values ($0.01 < \mathrm{Re}_K < 2$), and turbulent diffusion for large values

565   ($\mathrm{Re}_K > 2$).

566   Chandler et al.'s dataset allows us to quantitatively compare the performance of

567   the three diffusivity profiles (C, E, and C2E) over a Permeability Reynolds Number range

568   (0.2 to 4.34) that spans dispersive and turbulent diffusive mixing regimes (note that the

569   E2M profile is not included in this list because, as noted in **Section 4.4**, this profile is

570   functionally equivalent to the E Profile in the context of Chandler et al.'s dataset). Based

571   on our earlier analysis of Chandler et al.'s Exp ID 20110613 we concluded that the E

572   Profile represents a substantial improvement over the C Profile (**Section 4.3**). This

573   conclusion extends to the rest of Chandler et al.'s experiments as well (compare blue and

574   red circles in **Figure 5**, inferred parameter values summarized in **Tables S2 – S5**). In all

575   cases, the E Profile's infinite bed model captures a larger fraction of data variance ($R^2 >$

576   99.5%, **Figure 5a**) and has substantially smaller RMSE values (**Figures 5b**). The E

577   Profile's AICc is also >10 units lower than the C Profile's AICc (**Figure 5c**) implying

578   that, despite its increased complexity (i.e., the C and E Profiles have one and two

579   unknown parameters, respectively) the E Profile is the more parsimonious model (Weijs

580   and Ruddell, 2020; Aho et al., 2014).

581   [Figure 5 goes about here]

582   The C2E Profile's infinite bed model also performs quite well, but is a problem

583   with the inferred values of its inverse depth-scale. Compared to the E Profile, the C2E

584   Profile's infinite bed model has consistently lower RMSE and AICC values (compare

585   crosses and red circles in **Figures 5b** and **5c**) and a slightly improved coefficient of

586   determination ($R^2 > 99.8\%$, **Figure 5a**). However, these improvements come at the cost of

587   a new parameter (the C2E's inverse depth scale, a_{C2E}) whose inferred values are poorly

588   constrained (coefficient of variation in excess of 40 for some experiments, see **Table S7**),

589   highly variable (varying over 1000-fold from experiment-to-experiment, see distribution

590   of values represented by the violin plot in **Figure 6a**) and, in some cases, not physically

591   meaningful (e.g., the implied depth over which the effective diffusivity decays for $y > \ell_t$

592   is $1/a_{C2E} \approx 20$ microns for the largest value of a_{C2E} indicated in **Figure 6a**). Inferred

593   values of the C2E Profile's other two parameters (effective diffusivity, $D_{eff,0}^{C2E}$, and depth of

594   constant mixing, ℓ_t) are strongly correlated ($R^2 = 0.93$ and 0.76) with the effective

595   diffusivity, $D^{\mathrm{E}}_{\mathrm{eff},0}$, and decay length-scale, $1/a_{\mathrm{E}}$, inferred from the E Profile (**Figure 6b**,

596   **6c**), implying that both models capture the same basic information about the vertical

597   structure of the effective diffusivity; namely that the diffusivity is larger at the SWI and

598   lower at depth. In summary, of the four profiles evaluated in this study and across the full

599   range of Permeability Reynolds Numbers evaluated here (including dispersive and

600   turbulent diffusive transport regimes, see horizontal axis of **Figure 5**) the E Profile is the

601   most parsimonious descriptor of the effective diffusivity's vertical structure.

602   [Figure 6 goes about here]

603   **5.2 Is the Flux-Gradient Diffusive Model an Accurate Representation of Turbulent**

604   **Solute Transport Through the Streambed?**

605   We have already shown that the E Profile's infinite bed model captures a large

606   percentage of the variance in Chandler et al.'s water column Rhodamine measurements

607   ($R^2 > 99.5\%$, **Figure 5a**) but this assessment is based on the same datasets used for model

608   calibration. A more rigorous test of the E Profile in particular, and the flux-gradient

609   diffusive model more generally, can be stated as follows: *are the same E Profile*

610   *parameter values obtained when the model is optimized with Rhodamine measured in the*

611   *water column versus when the model is optimized with Rhodamine measured in the*

612   *interstitial fluids of sediment bed?* Put another way, can the evolution of solute

613   concentrations in the interstitial fluids of the sediment bed be inferred from the evolution

614   of solute concentration in the water column, and vice versa?

615   The answer is a qualified "yes". Across all 20 of Chandler et al.'s experiments,

616   effective diffusivities $D_{\mathrm{eff},0}$ estimated from the water and sediment column data are

617   strongly correlated over a 1000-fold change in the magnitude of this parameter (**Figure**

618   **7a,** Pearson's correlation coefficient, $R = 0.867$). Values of the inverse depth-scale

619   inferred from the water and sediment column data are much less variable and not

620   significantly correlated (**Figure 7b**), but their respective log-means ($a = 10^{1.61 \pm 0.18}$ m^{-1} and

621   $a = 10^{1.70 \pm 0.08}$, respectively) are equal within error. The corresponding mean values

622   ($a_E = 44.0 \pm 18.5$ m^{-1} and $a = 51.4 \pm 9.71$ m^{-1}, respectively, obtained by applying equations

623   (S25a) and (S25b) in Supplemental Information) are also equal, within error, to the

624   inverse depth-scale estimated by Chandler et al. in their original publication ($a = 55$ m^{-1})

625   (Chandler et al., 2016). This inverse depth-scale corresponds to a "$1/e$-folding depth"

626   (i.e., the depth at which the E Profile's effective diffusivity declines to $1/e \approx 0.37$ of its

627   surficial value) of approximately 2 cm, which comports with field and laboratory

628   estimates for the thickness of the benthic biolayer (2 to 5 cm below the SWI) (Tomasek et

629   al., 2018; Knapp et al., 2017; Krause et al., 2017; Caruso et al., 2017; Trauth et al., 2014;

630   Harvey et al., 2013; Kessler et al., 2013; Zarnetske et al., 2011; Battin et al., 2008; Dahm

631   et al., 2002). Thus, turbulent mixing may play an outsized role in the biogeochemical

632   processing of nutrients and other contaminants in streambed and coastal sediments.

633   [Figure 7 goes about here]

634   While effective diffusivities inferred from data collected above and below the

635   SWI are strongly correlated, bias is evident for experiments with Permeability Reynolds

636   Numbers greater than the approximate threshold for a fully turbulent SWI, $\mathrm{Re}_K > 10^{0.3} = 2$

637   (Voermans et al., 2017) (**Figure 7a**). One possible explanation focuses on how Chandler

638   et al. measured Rhodamine concentrations in the interstitial fluids of the sediment bed.

639   Chandler et al.'s in-bed measurements of Rhodamine WT are taken at a "point" (sensing

640   volume ca., 0.23 cm^3) with fiber optic fluorometers, whereas our analytical framework

641   assumes that interstitial solute concentrations are horizontally averaged (**Section 2**).

642   Indeed, Chandler (2010) describes how measured time series of concentration in the

643   sediment were sensitive to fluorometer location and these differences appeared consistent

644   over time; i.e. tracer appeared to mix out of the streambed faster on one side of the tank

645   than on the other (ibid. pg. 173). These authors also document distinct and persistent

646   patterns of mean flow velocity within the tank (ibid. pg. 118) which would lead to

647   heterogeneous turbulence intensities and corresponding heterogeneous efflux across the

648   SWI at high Permeability Reynolds Numbers. To the extent that Chandler et al.'s point

649   measurements are not equal to horizontally averaged concentrations, the effective

650   diffusivities inferred from these data will suffer accuracy problems. Indeed, Chandler

651   (2010) noted an order of magnitude discrepancy in the timescale over which interstitial

652   Rhodamine WT concentration declined on opposite sides of the stirred tank—a

653   discrepancy that could induce order-of-magnitude inaccuracy in estimated sediment-side

654   diffusivities (the scale of disagreement seen in **Figure 7a**).

655   An alternative explanation is that the flux-gradient diffusive model (equation (1a))

656   is an imperfect descriptor of turbulent mass transfer in the interstitial fluids of the

657   sediment bed at high Permeability Reynolds Number—a conclusion supported by the

658   systematic loss of model performance (i.e., higher RMSE and lower AICc and R^2 values)

659   observed at large values of this dimensionless number (i.e., $Re_K > 1$, **Figure 5**). Indeed,

660   the flux-gradient description of momentum transfer across other types of "porous"

661   boundaries, such as vegetation canopies, can break down; i.e., significant momentum flux

662   can occur in the absence of a velocity gradient, the analog of a concentration gradient for

663   mass transfer (Ghisalberti and Nepf, 2002). However, such observations typically occur

664   in the dispersive transport regime ($0.01 < \mathrm{Re}_K < 2$) where our estimates of effective

665   diffusivity above and below the SWI are in general concordance (**Figure 7a**). It should

666   also be noted that, even for the highest Permeability Reynolds Numbers trialed here and

667   so long as the diffusivity is allowed to decay exponentially with depth, the flux-gradient

668   diffusive model still explains a large fraction of variance in water column measurements

669   of Rhodamine WT ($R^2 > 0.995$) (**Figure 5a**).

670   In summary, based on Chandler et al.'s laboratory measurements we can conclude

671   the flux-gradient diffusive model is a reasonable representation of turbulent mass transfer

672   in the interstitial fluids of the sediment bed*, provided that the vertical structure of the*

673   *effective diffusivity is correctly specified (e.g., with the E Profile)*. However, a systematic

674   loss of model performance is observed with increasing Permeability Reynolds Number in

675   the turbulent diffusive regime ($\mathrm{Re}_K > 2$) possibly reflecting non-idealities associated with

676   Chandler et al.'s experimental measurements, a more fundamental breakdown in the flux-

677   gradient diffusive model, or some combination thereof. Further studies along these lines,

678   particularly in field settings, are warranted.

679   **5.3 Can Laboratory Measurements of Turbulent Mixing across the SWI be**

680   **Extrapolated to Stream and Coastal Sediments?**

681   Translation of these results to the field requires "scaling relationships" from which the E

682   Profile's two parameters—the effective diffusivity and inverse depth-scale—can be

683   estimated. Over the years a number of researchers have reported that effective

684   diffusivities (inferred by fitting the C Profile's null model to flume measurements of

685   turbulent mixing across flat sediment beds) exhibit a quadratic dependence on the

686   Permeability Reynolds Number, $D_{\mathrm{eff},0}^{C} \propto \mathrm{Re}_K^2$ (Richardson and Parr, 1988; O'Connor and

687   Harvey, 2008; Grant et al., 2012; Voermans et al., 2018; Grant et al., 2018). As noted

688   earlier, the Permeability Reynolds Number is calculated from the shear velocity, u_*,

689   sediment bed permeability, K, and the kinematic viscosity of water, υ. Permeability can

690   be estimated from the grain diameter and porosity of unconsolidated sediments (e.g.,

691   using the Kozeny-Carmen equation (Kamaan et al., 2007)) while the kinematic viscosity

692   of water is determined primarily by temperature (Rumble, 2019). Several methods are

693   available for measuring the shear velocity (c.f., Johnson and Cowen, 2017) including a

694   force-balance approach that provides spatially averaged estimates from the depth, h_w, and

695   slope, S [-], of a stream: $u_* = \sqrt{g h_w S}$ where $g = 9.81$ m s^{-2} is gravitational acceleration.

696   Thus, if the E Profile's two parameters can be expressed in terms of the Permeability

697   Reynolds Number, such relationships might pave the way for a direct translation of

698   laboratory measurements to field applications.

699   [Figure 8 goes about here]

700   When log-transformed effective diffusivities are plotted against the log-

701   transformed Permeability Reynolds Number, a significant change in slope and intercept

702   (as represented by non-overlapping 95% confidence intervals in equation (12a)) is

703   evident around $\mathrm{Re}_K = 1$ (**Figure 8a**).

704
$$\log_{10}\left(D_{\mathrm{eff},0}^{\mathrm{E}},\ \mathrm{m}^2\mathrm{s}^{-1}\right) = \begin{cases} \left(-5.31\pm0.09\right)+\left(2.53\pm0.17\right)\times\log_{10}\mathrm{Re}_K,\ R^2=0.905,\ \mathrm{Re}_K<1 \\ \left(-5.57\pm0.06\right)+\left(0.99\pm0.15\right)\times\log_{10}\mathrm{Re}_K,\ R^2=0.440,\ \mathrm{Re}_K>1 \end{cases} \quad (12a)$$

705   The power-law exponent for the surficial effective diffusivity declines from 2.53 ± 0.17

706   in the dispersive regime ($\mathrm{Re}_K<1$) to 0.99 ± 0.15 in the turbulent diffusive regime

707   ($\mathrm{Re}_K>1$). Likewise, the scaling behavior of the inverse depth-scale transitions from a

708 constant value ($a = 10^{1.74 \pm 0.01}$ m^{-1}) to a weak inverse dependence on the Permeability

709 Reynolds Number ($a \propto \mathrm{Re}_K^{-0.32 \pm 0.08}$) (**Figure 8b**):

$$\log_{10}\left(a_{\mathrm{E}},\ \mathrm{m}^{-1}\right) = \begin{cases} 1.74 \pm 0.01,\ \mathrm{Re}_K < 1 \\ \left(1.69 \pm 0.02\right) - \left(0.32 \pm 0.08\right) \times \log_{10}\mathrm{Re}_K,\ R^2 = 0.18,\ \mathrm{Re}_K > 1 \end{cases} \quad (12b)$$

711 In the dispersive mixing regime ($\mathrm{Re}_K < 1$) the implied mixing depth, $1/a_{\mathrm{E}} \approx 2$ cm, is

712 between 4 and 130 times larger than the diameter of the glass spheres that make up the

713 sediment bed ($0.150 \leq d_g \leq 5$ mm, depending on the experiment) and about 20 times larger

714 than an estimate of the depth to which the time-averaged turbulent velocity boundary

715 layer penetrates into the streambed called the Brinkman Layer thickness, $\delta_b \approx 20\sqrt{K} = 0.9$

716 mm (Voerman et al.'s 2017). It is also about ten-fold less than the depth of the sediment

717 bed ($d_b = 20$ cm), implying that the inferred inverse depth scale is not a proxy for bed

718 depth. These comparisons raise the question: *what is the physical interpretation of the*

719 *inverse depth-scale?* Based on a model for mass exchange across the SWI by turbulent

720 pumping, Higashino et al. (2009) reported that, at depths of around 2 cm and for shear

721 velocities on the lower end of the range employed by Chandler et al. ($u_* = 0.01$ and

722 0.016 m s^{-1}), the root mean square vertical velocity of the interstitial pore fluids are

723 >10% of their value at the SWI (ibid, Figure 3). Thus, one plausible interpretation is that

724 the inverse depth-scale represents the surficial region of streambed over which tracer

725 mass is vigorously mixed by turbulent pumping.

726 **6 Conclusions**

727 In this paper we developed and tested a rigorous one-dimensional modeling framework,

728 based on Duhamel's Theorem, for predicting mass transfer across the SWI and in the

729   benthic biolayer of a turbulent stream. The framework allows for depth-varying

730   diffusivity profiles, accounts for the change in porosity across the SWI, and encodes two-

731   way coupling across the SWI, in which mass transfer into the water column from the

732   sediment bed alters the water column concentration which, in turn, alters the mass flux

733   from the water column to the sediment bed, and so on. We applied this theory to an

734   extensive set of previously published measurements of turbulent mixing across a flat

735   sediment bed in a closed stirred tank (Chandler et al., 2016) with the goal of evaluating

736   the performance of four diffusivity depth profiles (C, E, E2M, and C2E Profiles). Key

737   findings include: (1) the flux-gradient diffusive model is a reasonable representation of

738   turbulent mass transfer across the SWI and in the interstitial fluids of the sediment bed,

739   *provided that the vertical structure of the effective diffusivity is correctly specified*; (2)

740   Chandler et al.'s experiments are most consistent with an exponentially declining

741   diffusivity profile (i.e., the E Profile); (3) values of the E Profile's two parameters

742   (effective diffusivity at the SWI, $D_{\text{eff},0}^{\text{E}}$, and inverse depth-scale, a_{E}) vary with the

743   Permeability Reynolds Number, Re_{K} , a dimensionless number that incorporates bed shear

744   stress and sediment permeability; (4) the dependence on the Permeability Reynold

745   Number changes abruptly at $\text{Re}_{K} = 1$, reflecting different modes of mixing below

746   (turbulent dispersion, $D_{\text{eff},0}^{\text{E}} = 10^{-5.31\pm0.09} \text{Re}_{K}^{2.53\pm0.17}$ and $a_{\text{E}} = 10^{1.74\pm0.01}$) and above (turbulent

747   diffusion, $D_{\text{eff},0}^{\text{E}} = 10^{-5.57\pm0.06} \text{Re}_{K}^{0.99\pm0.15}$ and $a_{\text{E}} = 10^{1.69\pm0.02} \text{Re}_{K}^{-0.32\pm0.08}$) this threshold value; (5)

748   the effective diffusivity's $1/e$ -folding depth is approximately 2 cm, consistent with the

749   hypothesis that solute mixing in the interstitial fluids of the sediment bed is facilitated

750   primarily by turbulent pumping; and (6) this $1/e$ -folding depth is also concordant with

751 field and laboratory measurements of the benthic biolayer thickness, implying that

752 turbulent mixing, and in particular turbulent pumping, may play an outsized role in the

753 biogeochemical processing of nutrients and other contaminants in streambed and coastal

754 sediments. Studies are presently underway to extend these findings to mixing across the

755 SWI by bedform pumping and bedform turnover with the ultimate goal of informing

756 pollutant fate and transport in coastal sediments and streams at catchment-to-continental

757 scales (Schmadel et al., 2019; Grant et al., 2018; Gomez-Velez et al., 2015; Gomez-Velez

758 and Harvey, 2014).

References.

779

780 Aho, K., Derryberry, D., & Peterson, T. (2014), Model selection for ecologists: the
781 worldviews of AIC and BIC. *Ecology*, 95(3), 631-636. doi:10.1890/13-1452.1

782 Azizian, M., Boano, F., Cook, P.L.M., Detwiler, R.L., Rippy, M.A., & Grant, S.B.
783 (2017), Ambient groundwater flow diminishes nitrate processing in the hyporheic zone of
784 streams, *Water Resources Research*, 53, doi:10.1002/2016WR020048.

785 Battin, T. J., Kaplan, L. A., Findlay, S., Hopkinson, C. S., Martí, E., Packman, A. I., et al.
786 (2008), Biophysical controls on organic carbon fluxes in fluvial networks. *Nature*
787 *Geoscience*, 1(2), 95–100. doi:10.1038/ngeo101

788 Boano, F., Revelli, R, & Ridolfi, L. (2011), Water and solute exchange through flat
789 streambeds induced by large turbulent eddies. *J. Hydrol*ogy, 402, 290-296.

790 Boano, F., Harvey, J. W., Marion, A., Packman, A. I., Revelli, R., Ridolfi, L., &
791 Wörman, A. (2014), Hyporheic flow and transport processes: Mechanisms, models, and
792 biogeochemical implications. *Reviews of Geophysics*, 52, 603-679.
793 doi:10.1002/2012RG000417

794 Bottacin-Busolin, A. (2019), Modeling the effect of hyporheic mixing on stream solute
795 transport. *Water Resource Research*. 55, 9995-10011. doi: 10.1029/2019WR025697

796 Breugem, W. P., Boersma, B. J., & Uittenbogaard, R. E. (2006). The influence of wall
797 permeability on turbulent channel flow. *Journal of Fluid Mechanics*, 562, 35–72.

798 Cardenas, M., J. L. Wilson, & R. Haggerty (2008), Residence time of bedform-driven
799 hyporheic exchange. *Advances Water Research*, 31, 1382-1386.

800 Caruso, A., F. Boano, L. Ridolfi, D. L. Chopp, & A. Packman (2017), Biofilm-induced
801 bioclogging produces sharp interfaces in hyporheic flow, redox conditions, and microbial
802 community structure, *Geophys. Res. Lett.*, 44, 4917–4925, doi:10.1002/2017GL073651.

803 Chandler, I.D. (2012), "Vertical variation in diffusion coefficient within sediments", PhD
804 thesis, Univ of Warwick, Coventry, U.K.

805 Chandler, I.D., Guymer, I., Pearson, J.M., & Egmond, R.V. (2016), Vertical variation of
806 mixing within porous sediment beds below turbulent flows. *Water Resources Research*,
807 52, 3493-3509. doi.org/10.1002/2015WR018274

808 Dahm, C. N., Grimm, N. B., Marmonier, P., Valett, H. M., & Vervier, P. (2002), Nutrient
809 dynamics at the interface between surface waters and groundwaters. *Freshwater Biology*,
810 40(3), 427–451. doi:10.1046/j.1365-2427.1998.00367.x

811 Elliott, A. H., & N. H. Brooks (1997a), Transfer of nonsorbing solutes to a streambed
812 with bed forms: Theory, *Water Resources Research*, 33, 123–136.

813 Elliott, A. H., & N. H. Brooks (1997b), Transfer of nonsorbing solutes to a streambed
814 with bed forms: Laboratory experiments. *Water Resources Research*, 33, 137–151.

815 Fleckenstein, J.H., Krause, S., Hannah, D.M., Boano, F. (2010), Groundwater-surface
816 water interactions: New methods and models to improve understanding of processes and
817 dynamics. *Adv. Water Resources*, 33, 1291-1295.

818   Franca, M.J. & Brocchini, M. (2015), Turbulence in Rivers. In P. Rowinski & A.
819   Radecki-Pawlick (Eds.), *Rivers—Physical, Fluvial, and Environmental Processes,*
820   GeoPlanet: Earth and Planetary Sciences, doi:10.1007/978030319-17719-9_2 (pp. 51–
821   78). Springer International Publishing, Switzerland.

822   Garcia, M.H. (2008), Sediment transport and morphodynamics, Sediment Engineering:
823   Processes, measurements, modeling, and practice. ASCE Manual No 110, Am. Soc. Of
824   Civ. Eng., ISBN 10 # 0784408149. doi:10.1061/40856(200)94

825   Ghisalberti, M., Nepf, H.M. (2002), Mixing layers and coherent structures in vegetated
826   aquatic flows. *J. Geophysical Research: Oceans*, 107, 3011. coi:10.1029/2001JC000871

827   Graf, U. (2004) "Applied Laplace Transforms and z-Transforms for Scientists and
828   Engineers—A Computational Approach using a Mathematica Package", New York, NY,
829   Springer-Basal AG, 1st Ed.

830   Grant, S. B. & Marusic, I. (2011), Crossing Turbulent Boundaries: Interfacial Flux in
831   Environmental Flows. *Environmental Science and Technology*, 45, 7107-7113.
832   doi:10.1021/es201778s

833   Grant, S. B. Stewardson, M. J. & Marusic, I. (2012), Effective diffusivity and mass flux
834   across the sediment-water interface in streams. *Water Resources Research*, 48, W05548.
835   doi:10.1029/2011WR011148

836   Grant, S. B., Stolzenbach, K., Azizian, M., Stewardson, M. J., Boano, F., & Bardini, L.
837   (2014), First-Order Contaminant Removal in the Hyporheic Zone of Streams: Physical
838   Insights from a Simple Analytical Model. *Environmental Science and Technology*, 48,
839   11369-11378. doi:10.1021/es501694k

840   Grant, S. B., Azizian, M., Cook, P., Boano, F. & Rippy, M. A. (2018a), Factoring stream
841   turbulence into global assessments of nitrogen pollution. *Science*, 359, 1266-1269.
842   https//doi:10.1126/science.aap8074

843   Grant, S.B. Gomez-Velez, J.D., & Ghisalberti, M. (2018b), Modeling the effects of
844   turbulence on hyporheic exchange and local-to-global nutrient processing in streams.
845   *Water Resources Research*, 54, doi:10.1029/2018WR023078.

846   Gomez-Velez, J. D., & Harvey, J. W. (2014), A hydrogeomorphic river network model
847   predicts where and why hyporheic exchange is important in large basins. *Geophysical*
848   *Research Letters*, 2014GL061099. doi:10.1002/2014GL061099

849   Gomez-Velez, J. D., Harvey, J. W., Cardenas, M. B., & Kiel, B. (2015), Denitrification in
850   the Mississippi River network controlled by flow through river bedforms. *Nature*
851   *Geoscience*, 8, 941-945. doi:10.1038/ngeo2567

852   Hall, R.O., Tank, J.L., Sobata, D.J., et al. (2009), Nitrate removal in stream ecosystems
853   measured by ^{15}N addition experiments: total uptake. *Limnology and Oceanography*, 43,
854   653-665.

855   Harvey, J. W., Böhlke, J. K., Voytek, M. A., Scott, D., & Tobias, C. R. (2013),
856   Hyporheic zone denitrification: Controls on effective reaction depth and contribution to
857   whole-stream mass balance. *Water Resources Research*, 49(10), 6298–6316.
858   doi:10.1002/wrcr.20492

859 Herzog, S.P., Higgins, C.P, Singha, K., & McCray, J.E. (2018), Performance of
860 engineered streambeds for inducing hyporheic transient storage and attenuation of
861 resazurin. *Environmental Science & Technology* 52, 10627-10636.

862 Hester, E. T., Cardenas, M. B., Haggerty, R., & Apte, S. V. (2017), The importance and
863 challenge of hyporheic mixing. *Water Resources Research*, 53(5), 3565–3575.
864 doi:10.1002/2016WR020005

865 Higashino, M.J., Clark, J., & Stefan, H. (2009) Pore water flow due to nearbed turbulence
866 and associated solute transfer in a stream or lake sediment bed. *Water Resources*
867 *Research* 45, W12414. doi:10.1029/2008WR007374

868 Hondzo, M. (1998), Dissolved oxygen transfer at the sediment-water interface in a
869 turbulent flow. *Water Resources Research*, 34(12), 3525-3533.

870 Iversen, N, & Jorgensen, B.B. (1993), Diffusion coefficients of sulfate and methane in
871 marine sediments: Influence of porosity. *Geochemica et Cosmochimica Acta*, 57, 571-
872 578.

873 Incropera, F.P., D.P. Dewitt, T.L. Bergman, & A.S. Lavine (2007), Fundamentals of Heat
874 and Mass Transfer, John Wiley, Hoboken, NJ.

875 Johnson, E.D., Cowen, E.A. (2017), Estimating bed shear stress from remotely measured
876 surface turbulent dissipation fields in open channel flows. *Water Resources Research*, 53,
877 1982-1996. doi:10.1002/2016WR018898

878 Kamann, P.J., Ritzi, R.W., Dominic, D.F., Conrad, C.M. (2007), Porosity and
879 permeability in sediment mixtures. *Ground Water* 45, 429-438.

880 Kessler, A.J., Glud, R.N., Cardenas, M.B., & Cook, P.L.M. (2013), Transport zonation
881 limits coupled nitrification-denitrification in permeable sediments. *Environmental*
882 *Science and Technology*, 47, 13404-13411.

883 Kim, T., Blois, G., Best, J., & Christensen, K. (2020). Experimental evidence of
884 amplitude modulation in permeable-wall turbulence. Journal of Fluid Mechanics, 887,
885 A3. doi:10.1017/jfm.2019.1027

886 Knapp, J.L.A., Gonzalez, Pinzon, R., Drummond, J.D., Larsen, L.G., Cirpka, O.A., &
887 Harvey, J.W. (2017), Tracer-based characterization of hyporheic exchange and benthic
888 biolayers in streams. *Water Resources Research*, 53, 1575-1594.
889 doi:10.1002/2016WR019393

890 Krause, S., Lewandowski, J., Grimm, N. B., Hannah, D. M., Pinay, G., McDonald, K., et
891 al. (2017), Ecohydrological interfaces as hot spots of ecosystem processes. *Water*
892 *Resources Research*, 53(8), 6359–6376. doi:10.1002/2016WR019516

893 Laube, G., Schmidt, C., & Fleckenstein, J.H. (2018), The systematic effect of streambed
894 conductivity heterogeneity on hyporheic flux and residence time. *Advances Water*
895 *Research*, 122, 60-69.

896 Leij, F.J., Priesack, E., Schaap, M.G. (2000), Solute transport modeled with Green's
897 functions with application to persistent solute sources. J. *Contaminant Hydrology* 41,
898 155-173.

899 Marion A., & M. Zaramella (2015) Diffusive behavior of bedform-induced hyporheic
900 exchange in rivers. *J. Environ. Eng.*, 131(9), 1260-1266. doi:10.1061/(ASCE)0733-
901 9372(2005)131:9(1260).

902 Myers, G.E. (1971), Analytical methods in conduction heat transfer, McGraw-Hill, New
903 York.

904 Nagaoka, H., & Ohgaki, S. (1990), Mass transfer mechanism in a porous riverbed. *Water*
905 *Research* 24(4), 417-425.

906 Newcomer, M.E., Hubbard, S.S., Fleckenstein, J.H., Maier, U., Schmidt, C., Thullner,
907 M., et al. (2016), Simulating bioclogging effects on dynamic riverbed permeability and
908 infiltration. *Water Resources Research*, 52(4), 2883-2900.
909 doi.org/10.1002/2015WR018351

910 O'Connor, B.L. & Harvey, J.W. (2008), Scaling hyporheic exchange and its influence on
911 biogeochemical reactions in aquatic ecosystems. *Water Resources Research*, 44,
912 W12423. doi:10.1029/2008WR007160

913 O'Connor, B.L., Harvey, J.W., & McPhillips, L.E. (2012), Thresholds of flow-induced
914 bed disturbances and their effects on stream metabolism in an agricultural river. *Water*
915 *Resources Research*, 48, W08504. doi:10.1029/2011WR011488

916 O'Connor, B.L., & Hondzo, M. (2008), Dissolved oxygen transfer to sediments by sweep
917 and eject motions in aquatic environments. *Limnology and Oceanography*, 53(2), 566-
918 578.

919 Packman, A.I., M. Salehin, M., & Zaramella, M. (2004), Hyporheic exchange with gravel
920 beds: Basic hydrodynamic interactions and bedform-induced advective flows. *ASCE J.*
921 *Hydraulic Engineeering.*, 130(7), 647-656.

922 Perez Guerrero, J.S., Pontedeiro, E.M. van Genuchten, M.Th., Skaggs, T.H. (2013),
923 Analytical solutions of the one-dimensional advection-dispersion solute transport
924 equation subject to time-dependent boundary conditions. *Chemical Engineering Journal*,
925 221, 487-491.

926 Pokrajac, D., & C. Manes (2009), Velocity measurements of a free-surface turbulent flow
927 penetrating a porous medium composed of uniform-size spheres, *Transp. Porous Med.*
928 78(3), 367–383, doi:10.1007/s11242-009-9339-8.

929 Pope, S.B. (2012), "Turbulent Flows", Cornell University, New York, U.S.A. doi:
930 10.1017/CB09780511840531

931 Reidenbach, M.A., Limm, M., Hondzo, M., & Stacey, M.T. (2010), Effects of bed
932 roughness on boundary layer mixing and mass flux across the sediment-water interface.
933 *Water Resources Research*, 46, W07530. doi:10.1029/2009WR008248

934 Richardson, C.P., & Parr, A.D. (1988), Modified Fickian model for solute uptake by
935 runoff. *ASCE J. Environmental Engineering*, 114, 792-809.

936 Roche, K.R., Blois, G., Best, J.L., Christensen, K.T., Aubeneau, A.F., & Packman, A.I.
937 (2018), Turbulence links momentum and solute exchange in coarse-grained streambeds.
938 *Water Resources Research*, 54, 3225-3242. doi:10.1029/2017WR021992

939 Roche, K.R., Li, A., Bolster, D., Wagner, G.J., & Packman, A.I. (2019), Effects of
940 turbulent hyporheic mixing on reach-scale transport. *Water Resources Research*, 55,
941 3780-3795.

942 Rumble, J. (Ed.) (2019) "CRC Handbook of Chemistry and Physics, 100th Ed." CRC
943 Press, Taylor and Francis Group, Boca Rotan, Florida.

944 Salehin, M., Packman, A.I., & Paradis, M. (2004), Hyporheic exchange with
945 heterogeneous streambeds: Laboratory experiments and modeling. *Water Resources*
946 *Research*, 40, W11504.

947 Schmadel, N.M., Harvey, J.W., Schwarz, G.E., Alexander, R.B., Gomez-Velez, J.D.,
948 Scott, D., & Ator, S.W. (2019), Small ponds in headwater catchments are a dominant
949 influence on regional nutrient and sediment budgets, *Geophysical Research Letters*,
950 46(16), 9669-9677. doi: 10.1029/2019GL083937

951 Stewardson, M.J., Datry, T., Lamouroux, N., Pella, H., Thommeret, N., Valette, L.,
952 Grant, S.B. (2016), Variation in reach-scale hydraulic conductivity of streambeds.
953 *Geomorphology*, 259, 70-80.

954 Thibodeaux, L.J., & Boyle, J.D. (1987), Bedform-generated convective transport in
955 bottom sediment. *Nature*, 325, 341-343.

956 Thibodeaux, L.J., Matisoff, G., Reible, D.D. (2011), "Bioturbation and Other Sorbed-
957 Phase Transport Processes in Surface Soils and Sediments", in *Handbook of Chemical*
958 *Mass Transport in the Environment* (L.J. Thibodeaux, D. Mackay, Eds.), CRC Press,
959 Taylor and Francis Group, Boca Raton, U.S.A.

960 Tomasek, A.A., Barman, T.D., Wang, P., Kozarek, J.L., Staley, C., Sadowsky, M.J., &
961 Hondzo, M. (2018). The effects of turbulence and carbon amendments on nitrate uptake
962 and microbial gene abundances in stream sediment. *J. Geophysical Research:*
963 *Biogeoscience*, 123, 1289-1301. https//doi:10.1002/2017JG004261

964 Trauth, N., Schmidt, C. Vieweg, M., Maier, U., & Fleckenstein, J. H. (2014), Hyporheic
965 transport and biogeochemical reactions in pool-riffle systems under varying ambient
966 groundwater flow conditions. *Journal Geophysical Research: Biogeosciences*, 119, 910-
967 928. https//doi:10.1002/2013JG002586

968 Voermans, J. J., Ghisalberti, M., & Ivey, G. N. (2017), The variation of flow and
969 turbulence across the sediment-water interface. *Journal of Fluid Mechanics*, 824, 413-
970 437. https//doi:10.1017/jfm.2017.345

971 Voermans, J. J., Ghisalberti, M., & Ivey, G. N. (2018), A model for mass transport across
972 the sediment-water interface. *Water Resources Research*, 54, 2799-2812.
973 https//doi:10.1002/2017WR022418

974 Weijs, S.V., Ruddell, B.L. (2020), Debates: Does Information Theory Provide a New
975 Paradigm for Earth Science? Sharper Predictions Using Occam's Digital Razor. *Water*
976 *Resources Research*, 56, e2019Wr026471. doi: 10.1029/2019WR026471

977 Wolke, P., Teitelbaum, Y., Deng, C., Lewandowski, J., Arnon, S. (2020), Impact of bed
978 form celerity on oxygen dynamics in the hyporheic zone. Water 12, 62.
979 https//doi.10.3390/w12010062

980   Wörman, A., (2000), Comparison of models for transient storage of solutes in small
981   streams. *Water Resources Research* 36(2), 455-468. doi:10.1029/1999WR900281

982   Zarnetske, J. P. Haggerty, R., Wondzell, S. M., & Baker, M. A. (2011), Dynamics of
983   nitrate production and removal as a function of residence time in the hyporheic zone.
984   Journal of *Geophysical Research: Biogeosciences*, 116(G1), G01025.
985   https//doi:10.1029/2010JG001356

986   Zheng, L., Cardenas M.B., Wang, L., & Mohrig, D. (2019) Ripple effects: bedform
987   morphodynamics cascading into hyporheic zone biogeochemistry. *Water Resources*
988   *Research,* Advanced online publication. https//doi:10.1029/29018WR023517

989   Zhong, Q., Chen, Q., Wang, H., Li, D., Wang, X. (2016), Statistical analysis of turbulent
990   super-streamwise vortices based on observations of streaky structures near the free
991   surface in the smooth open channel flow. *Water Resources Research*, 52, 3563–3578.
992   https//doi:10.1002/2015WR017728

Figure Captions.

Figure 1. (**a**) An illustration of how water column turbulence can influence mass

transport in the benthic biolayer. In this diagram, the benthic biolayer consists of a flat

coarse-grained streambed subject to turbulent pumping (traveling pressure wave, dashed

blue line), turbulence penetration (red eddies), and a time-averaged turbulent velocity

boundary layer that crosses the sediment-water interface (envelope of black arrows). The

vertical mass flux $J(y)$ arising from these turbulence-linked phenomena is assumed to

follow the flux-gradient diffusive model (equation (1a)). (**b**) Turbulent mixing across the

SWI can be measured in the laboratory using closed systems, such as a stirred tank. Two-

way coupling across the SWI is indicated by the two circular arrows.

Figure 2. Four functional forms of the effective diffusivity profile $f(y)$ trialed in this

study (equations (8a) through (8d)). Variables represent the depth into the sediment bed

(y), surficial effective diffusivity (at the SWI, $D_{eff,0}$), a mixing length-scale ($1/a$), and

the thickness of enhanced mixing at the surface of the sediment bed (ℓ_t).

Figure 3. The influence of two-way coupling and finite bed depth on the evolution of

solute concentration in the (**a**) water column and (**b**) interstitial fluids of the sediment

bed, assuming solute is initially present only in the interstitial fluids of the sediment bed

and the diffusivity profile is constant with depth (C Profile). See text for details.

Figure 4. Chandler et al.'s water (top panels) and sediment (bottom panels) column data

compared to infinite bed model predictions for the (**a**) C Profile, (**b**) E Profile, and (**c**) C2E

Profile. Black curves are model-predicted solute concentration in the water column (top

panel) and at two depths in the sediment bed (15 and 151 mm below the SWI, lower panel).

Blue horizontal lines represent the well-mixed (equilibrium) concentration (equation (9a)).

Data highlighted in red correspond to Chandler et al.'s Exp ID 20110613.

Figure 5. Performance of the C, E and C2E infinite bed models across all 20 of Chandler

et al.'s stirred tank experiments. Model performance metrics include: (**a**) coefficient of

determination, R^2; (**b**) Root Mean Square Error, RMSE; and (**c**) Akaike's Information

Criterion, AICc.

1022 **Figure 6**. An evaluation of C2E fitting parameters inferred from Rhodamine

1023 concentration in the water column for all twenty of Chandler et al.'s stirred tank

1024 experiments. (**a**) Values of C2E's inverse depth scale vary over three orders of

1025 magnitude, as illustrated here with a violin plot. The effective diffusivity (**b**) and depth of

1026 the constant mixing zone (**c**) inferred from the C2E profile model (vertical axes) are

1027 strongly correlated ($R^2 = 0.93$ and 0.76) with, respectively, the E Profile's effective

1028 diffusivity and inverse decay depth-scale (horizontal axes).

1029 **Figure 7**. A comparison of (**a**) effective diffusivities and (**b**) inverse depth-scales

1030 obtained by fitting the E Profile model to water column (vertical axis) or sediment

1031 column (horizontal axis) measurements of Rhodamine concentration. The points are

1032 colored to indicate the Permeability Reynolds Number.

1033 **Figure 8**. Permeability Reynolds Number scaling of the E Profile's two parameters

1034 estimated from Chandler et al.'s water column measurements. The surficial diffusivity (**a**)

1035 and inverse decay length-scale (**b**) follow different scaling relationships in the dispersive

1036 (blue lines) and turbulent diffusive (green lines) ranges. Dashed curves are 95%

1037 prediction intervals.

1038

1039

Table 1. Green's functions for various choices of the diffusivity depth profile and a finite

or semi-infinite sediment bed.[1]

C Profile, $f_{\mathrm{C}}(\bar{y})=1$
Semi-infinite Sediment Bed, $\bar{y}=a_{\mathrm{C}}y>0$, $\bar{s}=st_{\mathrm{T}}$
$\tilde{G}(\bar{y},\bar{s})=e^{-\bar{y}\sqrt{\bar{s}}}$, $\bar{y}>0$ (T-1)
Finite Sediment Bed, $\bar{y}=a_{\mathrm{C}}y>0$, $\bar{d}_b=d_b a_{\mathrm{C}}>0$, $\bar{y}<\bar{d}_b$, $\bar{s}=st_{\mathrm{T}}$
$\tilde{G}(\bar{y},\bar{s})=\dfrac{e^{-\bar{y}\sqrt{\bar{s}}}\left(e^{2\bar{d}_b\sqrt{\bar{s}}}+e^{2\bar{y}\sqrt{\bar{s}}}\right)}{1+e^{2\bar{d}_b\sqrt{\bar{s}}}}$ (T-2)
E Profile, $f_{\mathrm{E}}(\bar{y})=e^{-\bar{y}}$
Semi-infinite Sediment Bed, $\bar{y}=a_{\mathrm{E}}y>0$, $\bar{s}=st_{\mathrm{T}}$
$\tilde{G}(\bar{y},\bar{s})=\sqrt{e^{\bar{y}}}\,\dfrac{K_1\left(2\sqrt{\bar{s}e^{\bar{y}}}\right)}{K_1\left(2\sqrt{\bar{s}}\right)}$ (T-3)
E2M Profile, $f_{\mathrm{E2M}}(\bar{y})=\begin{cases} e^{-\bar{y}}, & 0\le\bar{x}\le\bar{\ell}_m \\ \bar{D}, & \bar{x}>\bar{\ell}_m \end{cases}$
Semi-infinite Sediment Bed, $\bar{y}=a_{\mathrm{E2M}}y>0$, $\bar{\ell}_m=-\ln\bar{D}$, $0<\bar{D}<1$, $\bar{D}=\dfrac{D'_m}{D^{\mathrm{E2M}}_{\mathrm{eff},0}}$, $\bar{s}=st_{\mathrm{T}}$
$\tilde{G}(\bar{y},\bar{s})=\begin{cases} \tilde{G}_1(\bar{y},\bar{s}), & \bar{y}\le-\ln\bar{D} \\ \tilde{G}_2(\bar{y},\bar{s}), & \bar{y}>-\ln\bar{D} \end{cases}$ (T-5a)
$\tilde{G}_1(\bar{y},\bar{s})=\sqrt{e^{\bar{y}}}\,\dfrac{I_1\left(2\sqrt{e^{\bar{y}}\bar{s}}\right)\left[K_0\left(2\sqrt{\tfrac{\bar{s}}{\bar{D}}}\right)-K_1\left(2\sqrt{\tfrac{\bar{s}}{\bar{D}}}\right)\right]+K_1\left(2\sqrt{e^{\bar{y}}\bar{s}}\right)\left[I_0\left(2\sqrt{\tfrac{\bar{s}}{\bar{D}}}\right)+I_1\left(2\sqrt{\tfrac{\bar{s}}{\bar{D}}}\right)\right]}{K_1\left(2\sqrt{\bar{s}}\right)\left[I_0\left(2\sqrt{\tfrac{\bar{s}}{\bar{D}}}\right)+I_1\left(2\sqrt{\tfrac{\bar{s}}{\bar{D}}}\right)\right]+I_1\left(2\sqrt{\bar{s}}\right)\left[K_0\left(2\sqrt{\tfrac{\bar{s}}{\bar{D}}}\right)-K_1\left(2\sqrt{\tfrac{\bar{s}}{\bar{D}}}\right)\right]}$ (T-5b)
$\tilde{G}_2(\bar{y},\bar{s})=\dfrac{e^{-(\bar{y}+\ln\bar{D})\sqrt{\tfrac{\bar{s}}{\bar{D}}}}}{\sqrt{\bar{D}}}\,\dfrac{I_1\left(2\sqrt{\tfrac{\bar{s}}{\bar{D}}}\right)K_0\left(2\sqrt{\tfrac{\bar{s}}{\bar{D}}}\right)+I_0\left(2\sqrt{\tfrac{\bar{s}}{\bar{D}}}\right)K_1\left(2\sqrt{\tfrac{\bar{s}}{\bar{D}}}\right)}{K_1\left(2\sqrt{\bar{s}}\right)\left[I_0\left(2\sqrt{\tfrac{\bar{s}}{\bar{D}}}\right)+I_1\left(2\sqrt{\tfrac{\bar{s}}{\bar{D}}}\right)\right]+I_1\left(2\sqrt{\bar{s}}\right)\left[K_0\left(2\sqrt{\tfrac{\bar{s}}{\bar{D}}}\right)-K_1\left(2\sqrt{\tfrac{\bar{s}}{\bar{D}}}\right)\right]}$ (T-5c)
C2E Profile, $f_{\mathrm{C2E}}(\bar{y})=\begin{cases} 1, & 0\le\bar{y}\le\bar{\ell}_t \\ e^{-\bar{y}}, & \bar{y}>\bar{\ell}_t \end{cases}$
Semi-infinite Sediment Bed, $\bar{y}=a_{\mathrm{C2E}}y>0$, $\bar{\ell}_t=a_{\mathrm{C2E}}\ell_t>0$, $\bar{s}=st_{\mathrm{T}}$
$\tilde{G}(\bar{y},\bar{s})=\begin{cases} \tilde{G}_1(\bar{y},\bar{s}), & \bar{y}\le\bar{\ell}_t \\ \tilde{G}_2(\bar{y},\bar{s}), & \bar{y}>\bar{\ell}_t \end{cases}$ (T-6a)

$$\tilde{G}_1(\bar{y},\bar{s}) = \frac{K_1\left(2\sqrt{\bar{s}}\right)\cosh\left[\sqrt{\bar{s}}\left(\bar{y}-\bar{\ell}_t\right)\right] - K_0\left(2\sqrt{\bar{s}}\right)\sinh\left[\sqrt{\bar{s}}\left(\bar{y}-\bar{\ell}_t\right)\right]}{K_1\left(2\sqrt{\bar{s}}\right)\cosh\left(\bar{\ell}_t\sqrt{\bar{s}}\right) + K_0\left(2\sqrt{\bar{s}}\right)\sinh\left(\bar{\ell}_t\sqrt{\bar{s}}\right)} \tag{T-6b}$$

$$\tilde{G}_2(\bar{y},\bar{s}) = \frac{e^{(\bar{y}-\bar{\ell}_t)/2}K_1\left(2e^{(\bar{y}-\bar{\ell}_t)/2}\sqrt{\bar{s}}\right)}{K_1\left(2\sqrt{\bar{s}}\right)\cosh\left(\bar{\ell}_t\sqrt{\bar{s}}\right) + K_0\left(2\sqrt{\bar{s}}\right)\sinh\left(\bar{\ell}_t\sqrt{\bar{s}}\right)} \tag{T-6c}$$

1042   [1]The functions K_0 , K_1 , and K_2 are Modified Bessel functions of the Second Kind, while

1043 I_0 , I_1 , and I_2 are Modified Bessel functions of the First Kind.
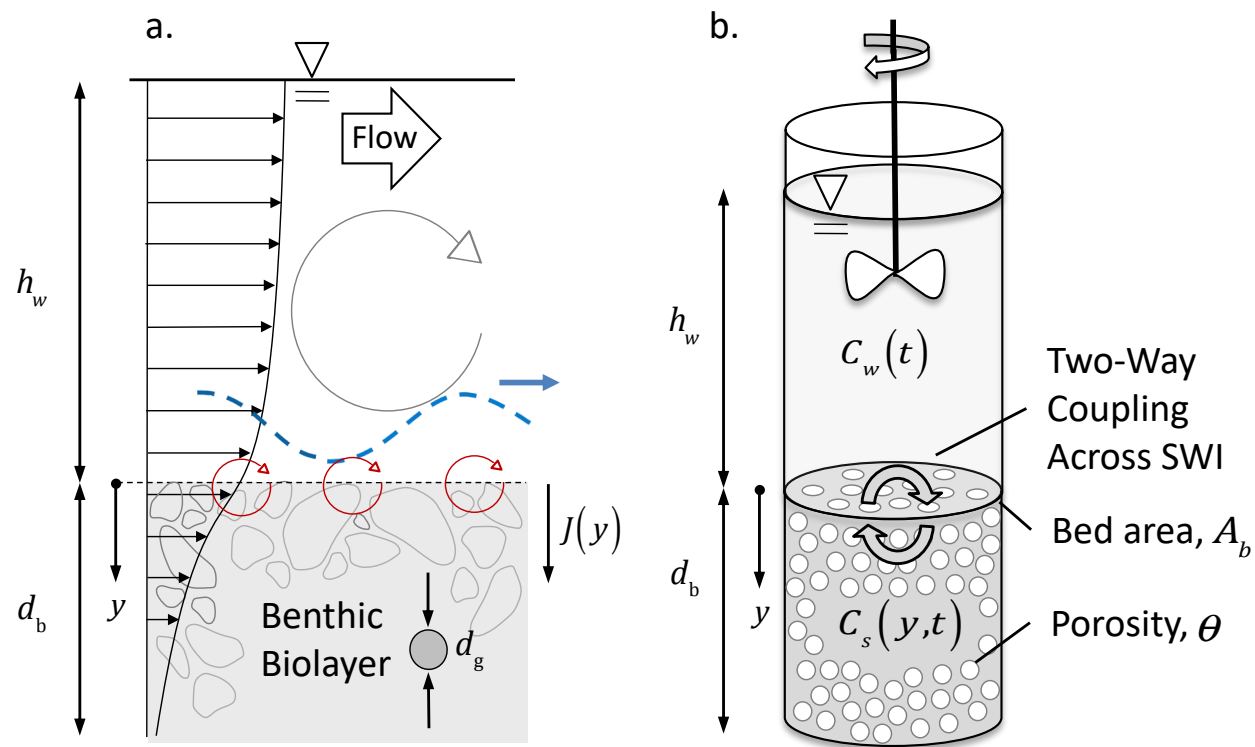
Figure 1. Grant et al. (2020)
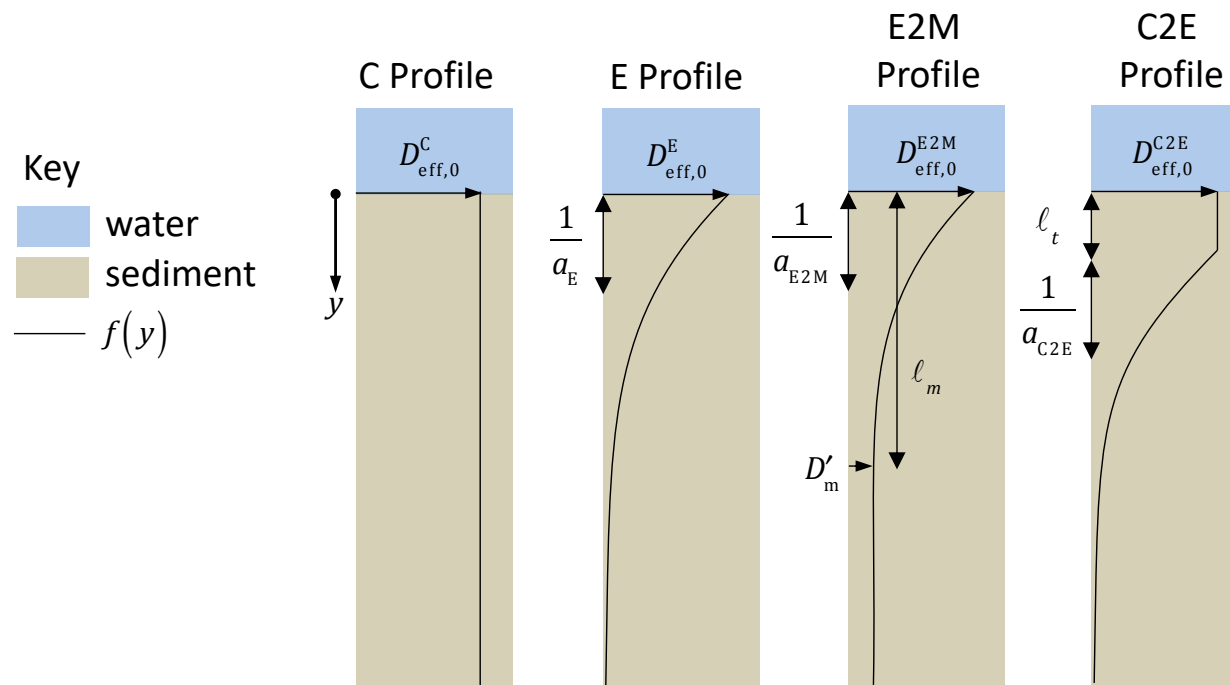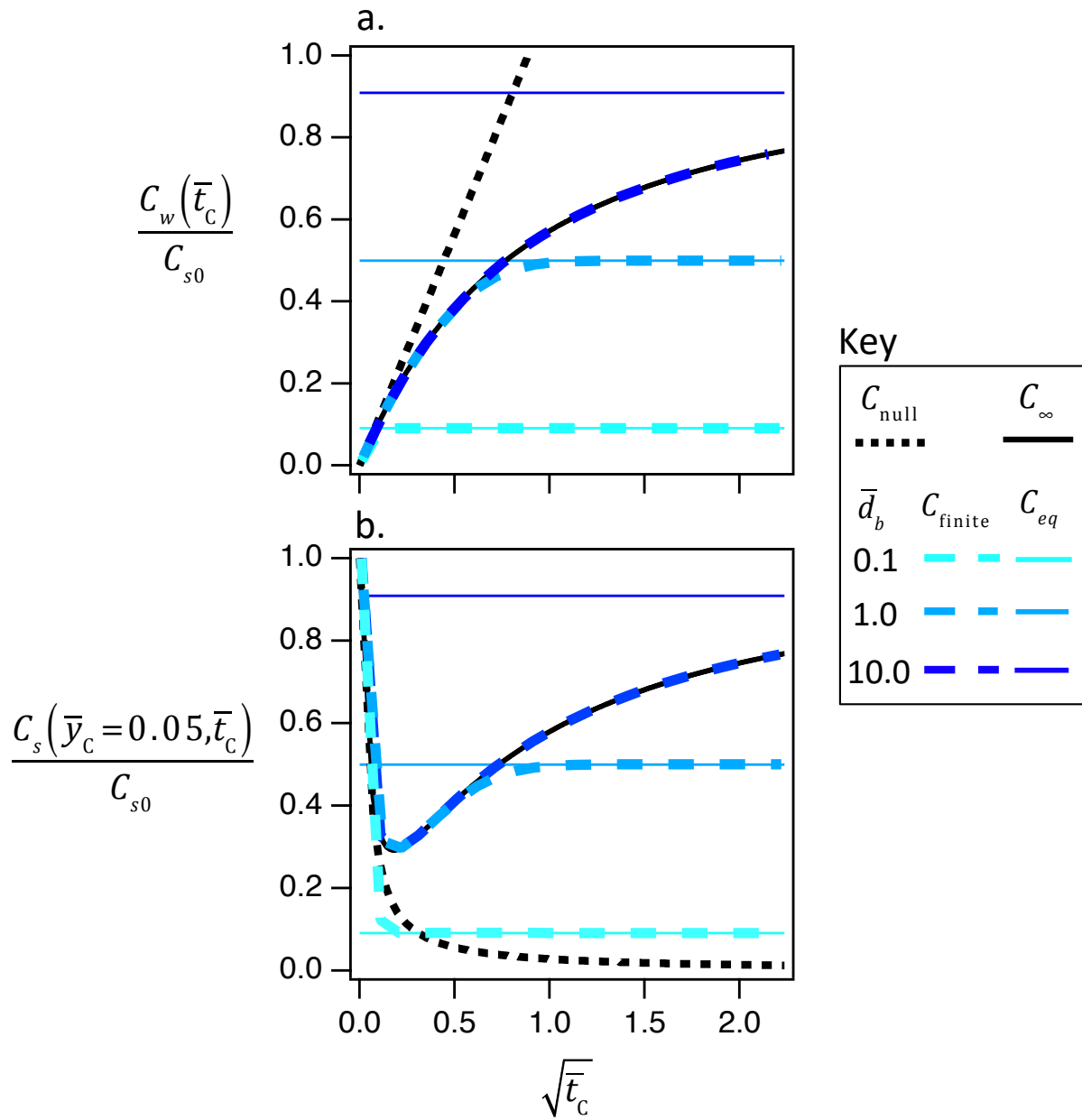
Figure 2. Grant et al. (2020)
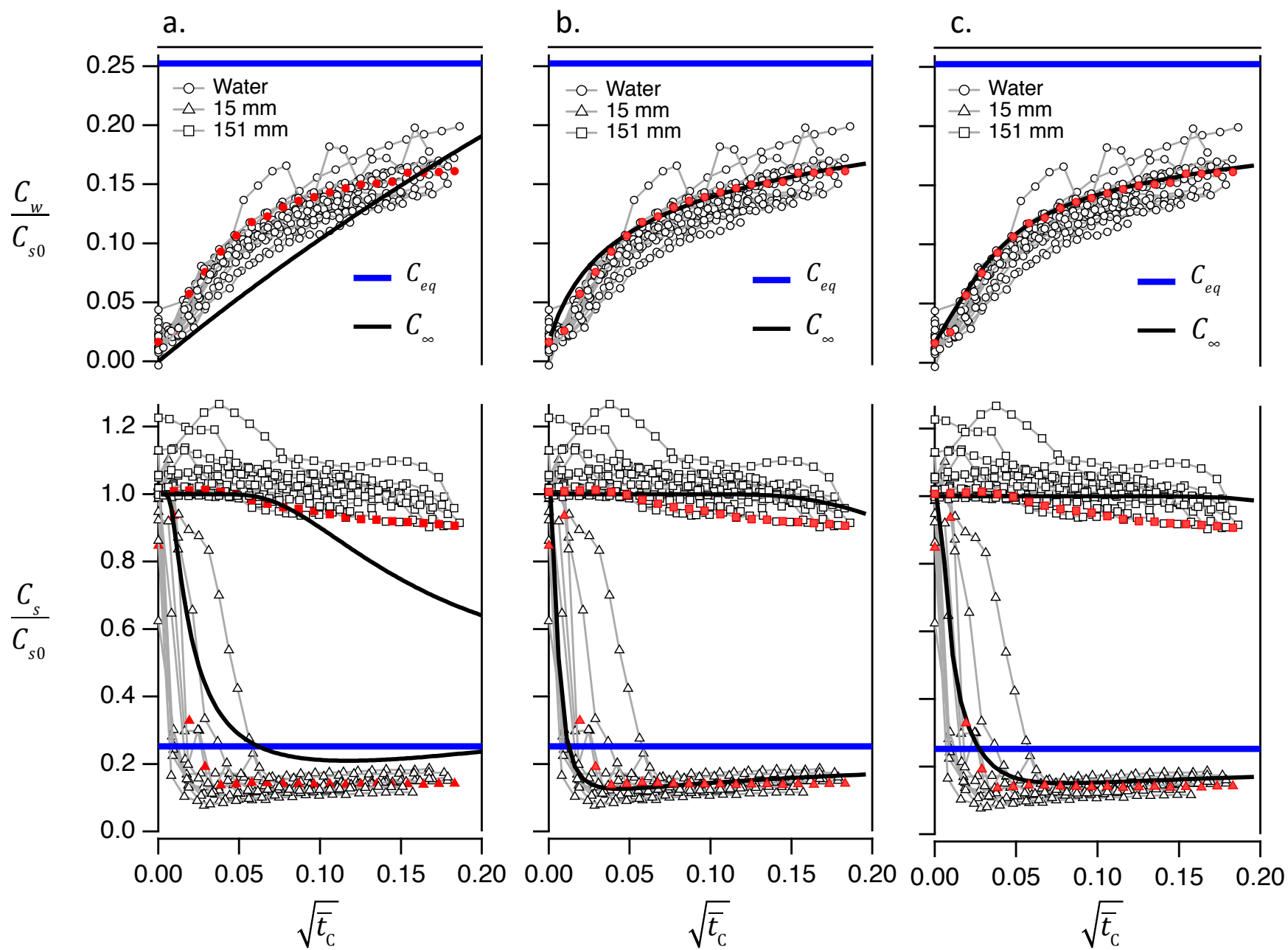
Figure 3. Grant et al. (2020)
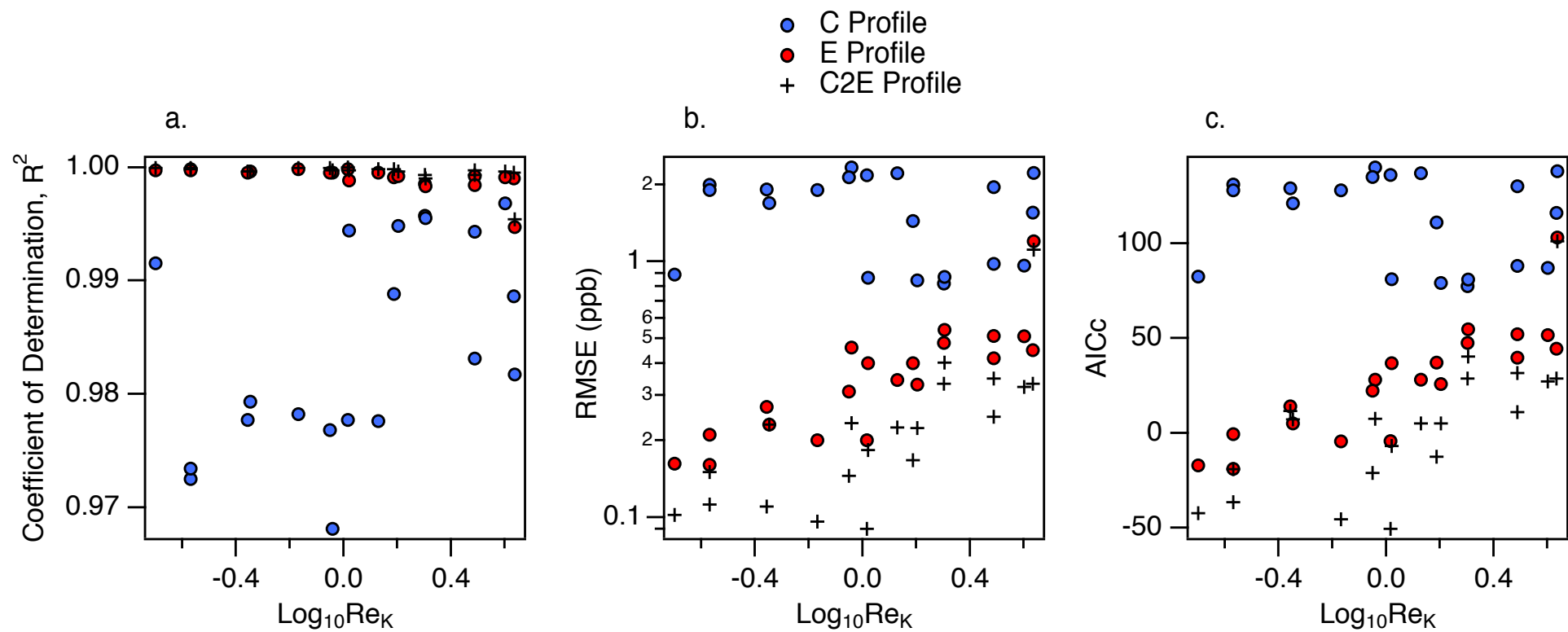
Figure 4. Grant et al. (2020)
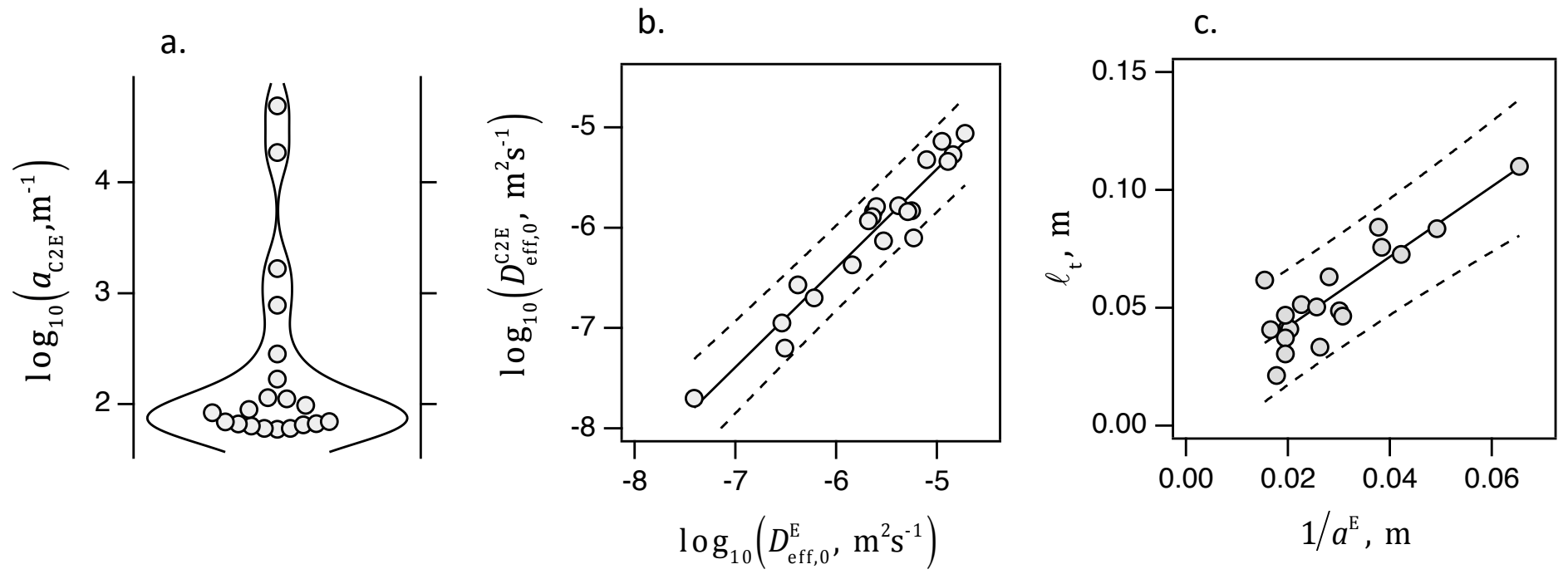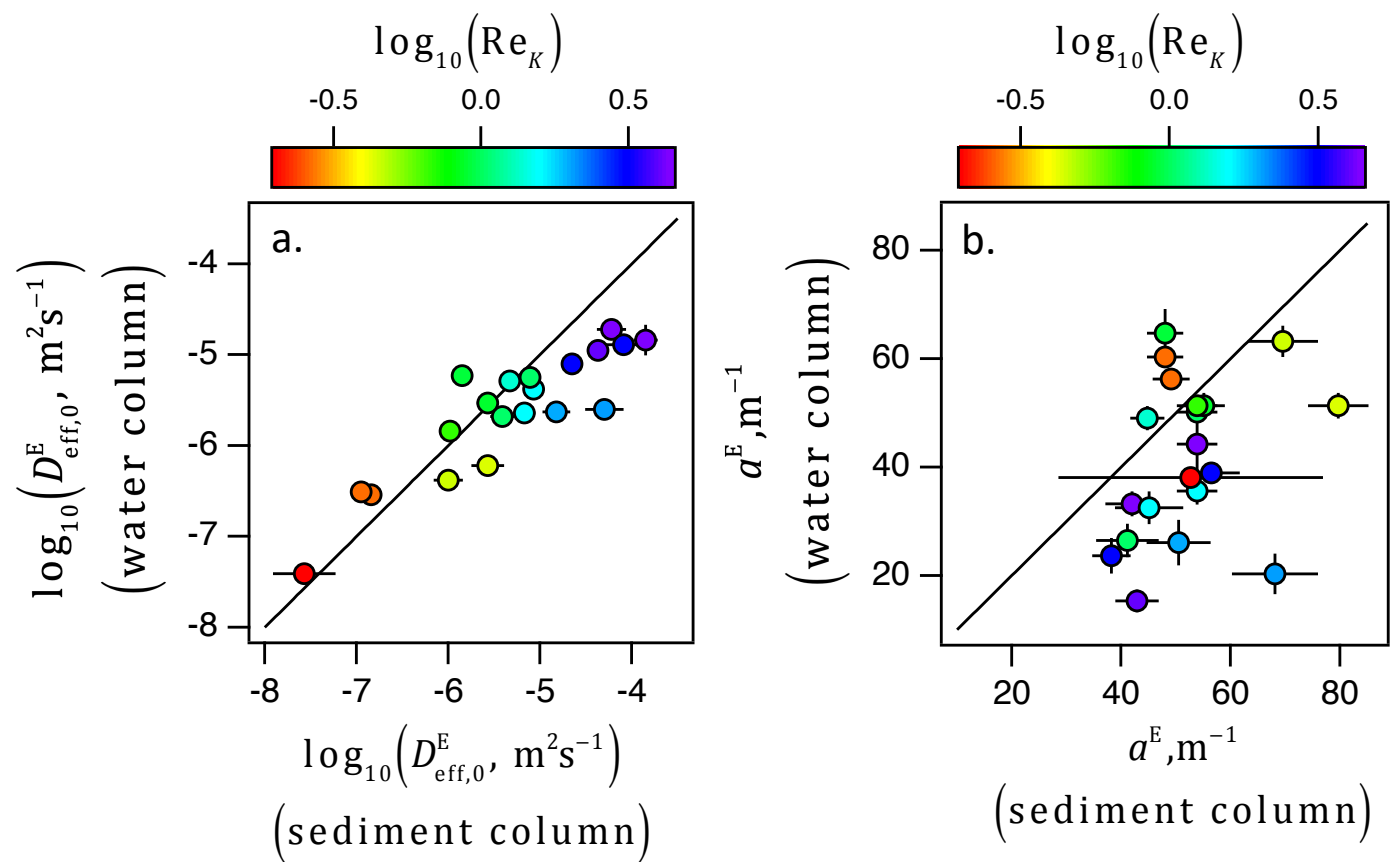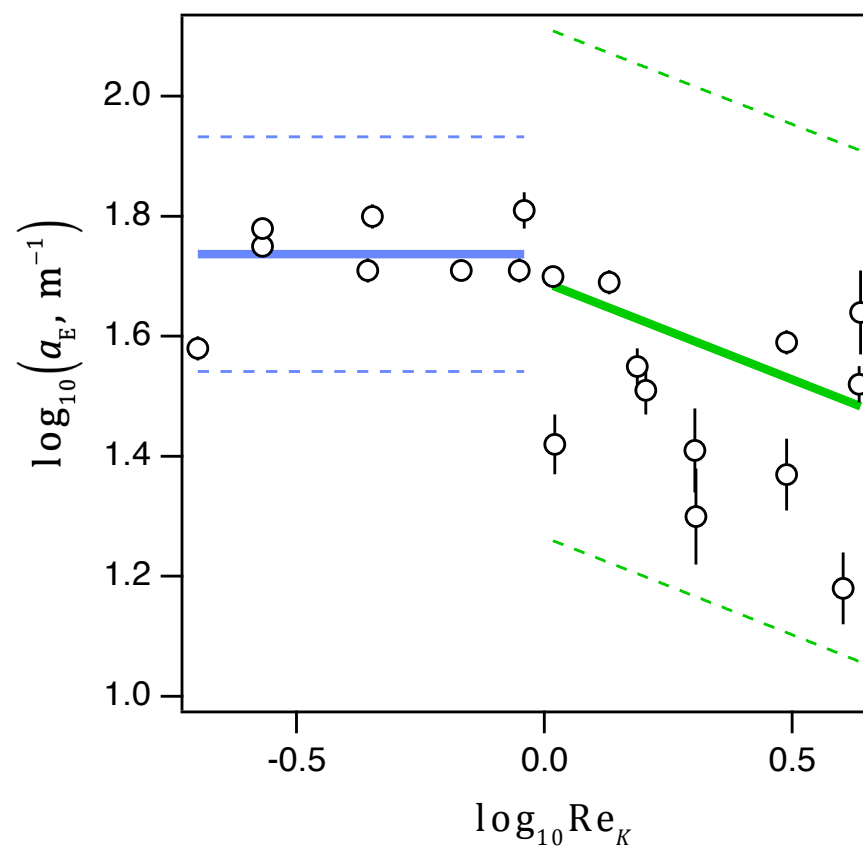
Figure 5. Grant et al. (2020)

a.

$\log_{10}\left(a_{\mathrm{C2E}}, \mathrm{m}^{-1}\right)$

b.

$\log_{10}\left(D_{\mathrm{eff,0}}^{\mathrm{C2E}}, \mathrm{m^2 s^{-1}}\right)$

$\log_{10}\left(D_{\mathrm{eff,0}}^{\mathrm{E}}, \mathrm{m^2 s^{-1}}\right)$

c.

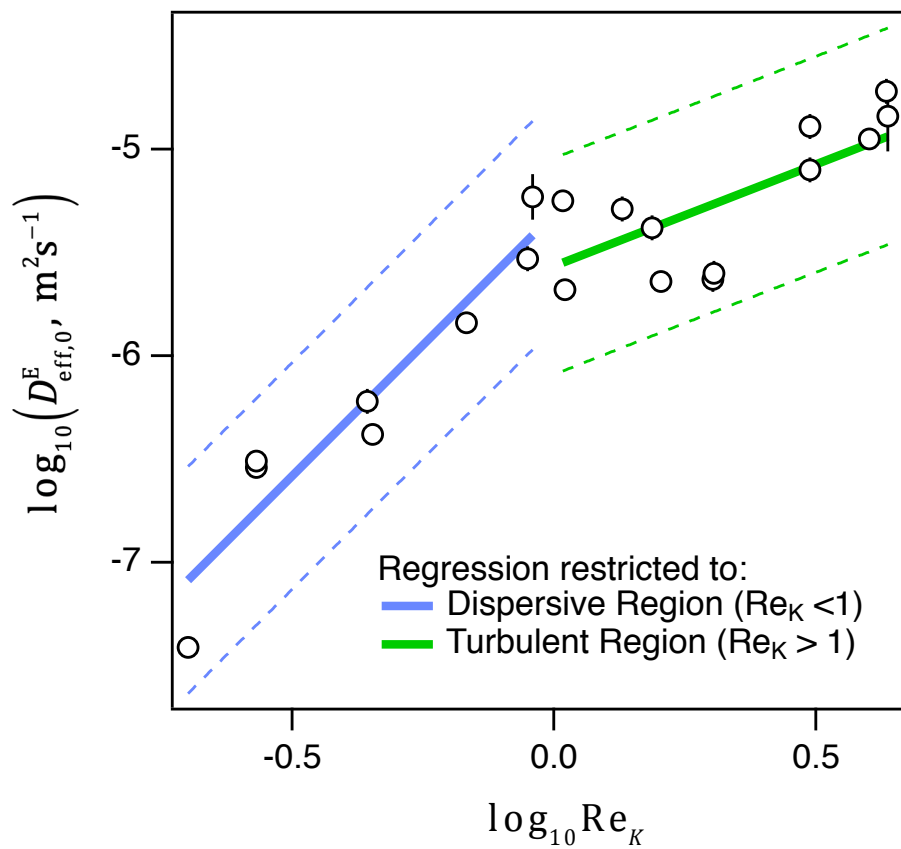ℓ_t, m

$1/a^{\mathrm{E}}$, m

Figure 6. Grant et al. (2020)

Figure 7. Grant et al. (2020)

Figure 8. Grant et al. (2020)